

③

REPORT DOCUMENTATION PAGE

Form Approved
OMB No 0704-0188
Exp Date Jun 30 1986

1a REPORT SECURITY CLASSIFICATION Unclassified		1b RESTRICTIVE MARKINGS FILE COPY	
AD-A209 247		3. DISTRIBUTION/AVAILABILITY OF REPORT Approved for public release; distribution unlimited	
DULE		5. MONITORING ORGANIZATION REPORT NUMBER(S)	
IBER(S)		7a NAME OF MONITORING ORGANIZATION U.S. Army Research Office	
6a NAME OF PERFORMING ORGANIZATION Brooklyn College of CUNY		7b ADDRESS (City, State, and ZIP Code) P.O. Box 12211 Research Triangle Park, NC 27709-2211	
6b OFFICE SYMBOL (if applicable)		9. PROCUREMENT INSTRUMENT IDENTIFICATION NUMBER	
8a NAME OF FUNDING / SPONSORING ORGANIZATION U.S. Army Research Office		10. SOURCE OF FUNDING NUMBERS	
8b OFFICE SYMBOL (if applicable)		PROGRAM ELEMENT NO.	
8c ADDRESS (City, State, and ZIP Code) P.O. Box 12211 Research Triangle Park, NC 27709-2211		PROJECT NO.	
		TASK NO.	
		WORK UNIT ACCESSION NO.	
11. TITLE (Include Security Classification) Raman Spectroscopy Study of Microstructural Geometries in Semiconductors			
12. PERSONAL AUTHOR(S) Prof. Fred H. Pollak			
13a. TYPE OF REPORT Final		13b. TIME COVERED FROM 4/15/85 TO 10/14/88	
14. DATE OF REPORT (Year, Month, Day) 1989, March 31		15. PAGE COUNT 76	
16. SUPPLEMENTARY NOTATION The view, opinions and/or findings contained in this report are those of the author(s) and should not be construed as an official Department of the Army position, policy, or decision, unless designated by other documentation.			
17. COSATI CODES		18. SUBJECT TERMS (Continue on reverse if necessary and identify by block number)	
FIELD	GROUP	SUB-GROUP	
		Raman Spectroscopy, Semiconductor Microstructures, HgCdTe	
		JES)	
19. ABSTRACT (Continue on reverse if necessary and identify by block number)			
<p>We report a program of the study of semiconductor microstructural geometries by Raman scattering (RS). From RS at 300K and photoluminescence at 4K we have deduced information about the alloy potential fluctuations in MBE fabricated $\text{Al}_{0.48}\text{In}_{0.52}\text{As/InP}$ grown at different substrate temperatures. A comparative study of RS, transmission electron microscopy (TEM) and conductivity has been performed on molecular beam deposited microcrystalline Si and Ge. A detailed analysis of the RS lineshape reveals that it is more sensitive to point defects (impurities) in relation to TEM. Information</p>			
20. DISTRIBUTION/AVAILABILITY OF ABSTRACT <input type="checkbox"/> UNCLASSIFIED/UNLIMITED <input type="checkbox"/> SAME AS RPT <input type="checkbox"/> DTIC USERS		21. ABSTRACT SECURITY CLASSIFICATION Unclassified	
22a NAME OF RESPONSIBLE INDIVIDUAL		22b TELEPHONE (Include Area Code)	
		22c OFFICE SYMBOL	

about the surface electric fields in heavily doped $\langle 100 \rangle$ n-GaAs has been obtained by studying the symmetry forbidden polarization configurations in RS. We have performed a detailed, comprehensive investigation of polish-induced surface strain in $\langle 100 \rangle$ and $\langle 111 \rangle$ GaAs and InP. Considerable information has been obtained about surface strain, strain skin-depth and diffusion of damage into the sample. *

A photoreflectance (PR) study of $\text{Hg}_{1-x}\text{Cd}_x\text{Te}$ fabricated by different growth conditions has demonstrated the utility of this method in evaluating crystal quality. In addition, by investigating the pump chopping frequency dependence of the PR, information was obtained about surface (interface) traps. The interface properties of $\text{Hg}_{0.7}\text{Cd}_{0.3}\text{Te}/\text{SiO}_2$ were studied by photo-and bias-induced charging. It was possible to detect very slow interface states and to gain information about their energy distribution.

RAMAN SPECTROSCOPY INVESTIGATION
OF MICROSTRUCTURAL GEOMETRIES
IN SEMICONDUCTORS

Final Report

Professor Fred H. Pollak

April 7, 1989

U.S. ARMY RESEARCH OFFICE
CONTRACT DAAG29-85-K-0076

Brooklyn College of CUNY

Accession For	
NTIS GRA&I	<input checked="" type="checkbox"/>
DTIC TAB	<input type="checkbox"/>
Unannounced	<input type="checkbox"/>
Justification	
By	
Distribution/	
Availability Codes	
Dist	Avail and/or Special
A-1	



FHP8905.bjm

TABLE OF CONTENTS

I. INTRODUCTION	1
II. EXPERIMENTAL RESULTS	3
A. Raman Spectroscopy Study of the Effect of Growth Conditions on Alloy Potential Fluctuations in $\text{Al}_{0.48}\text{In}_{0.52}\text{As/InP}$	3
B. Raman, Transmission Electron Microscopy and Conductivity Measurements of Molecular Beam Deposited Microcrystalline Si and Ge	8
C. Symmetry Forbidden LO-phonon Raman Scattering from Electric Fields in the Space Charge Region in Heavily Doped $\langle 100 \rangle$ n-GaAs.	12
D. Comprehensive Investigation of Polish-Induced Surface Strain in $\langle 100 \rangle$ and $\langle 111 \rangle$ GaAs and InP	17
E. Excitation Wavelength and Pump Chopping Frequency Dependence of Photoreflectance in $\text{Hg}_{1-x}\text{Cd}_x\text{Te}$	35
F. $\text{Hg}_{0.7}\text{Cd}_{0.3}\text{Te/SiO}_2$ -Photox Interface Properties Studied by Photo-and Bias-Induced Charging	38
REFERENCES	44
TABLES	49
FIGURES	54
III. PUBLISHED PAPERS	76

I. INTRODUCTION

Raman scattering (RS) is an extremely useful tool for studying semiconductors either in bulk or thin film form. RS depends on the electron-phonon interaction and therefore is an important complement to other spectroscopic techniques (ellipsometry, luminescence, modulated spectroscopy, various photo-electron spectroscopies, etc.) which are functions of the electron states of the solid. RS is one of the most important methods for studying the lattice vibration of a semiconductor and interactions with other excitations such as plasmons, magnons etc. Since lattice vibrations are very sensitive to local environments, RS can yield information about the semiconductor on the scale of a few lattice constants. Thus it is ideal for investigating the nature of microstructural geometries, i.e. structures which are of order $10 - 1000 \text{ \AA}$ in dimensions. Also since RS is a second-order process it contains important symmetry information not available from first-order optical interactions. In RS, both polarization selection rules as well as peak positions are sensitive to perturbations, both internal and external, such as strain, electric fields, temperature, etc. Furthermore by using various excitation lines with different wavelengths it is possible to (a) perform depth profiling measurements or (b) excite resonance interactions.

One of the most significant aspects of some of our initial results has been the demonstration the a "spatial correlation" model (SCM) with a Gaussian correlation function is a very general approach to q-vector relaxation in semiconductors due to a number of microstructural effects. This model has already been used to account for finite size effects in microcrystalline geometries but the most recent experiments show that it is also applicable to ion-damage material and alloy semiconductors. The detailed analysis of the Raman lineshape yields a physically significant parameter, i.e. the "spatial correlation length which can be related to the size of the microcrystalline region, the size of the ion-damage region in ion-damaged (and possible annealed) material or the size of the compositionally-ordered section of alloy semiconductors. The ability to extract this microscopic quantity from macroscopic measurements opens up new areas of investigation that are of significance from both a fundamental and technological point of view. Using the SCM we have analyzed the RS of the

alloy $\text{Al}_{0.48}\text{In}_{0.52}\text{As}/\text{InP}$ grown under different conditions including substrate temperature. Evidence for alloy ordering is found at a particular substrate temperature. Molecular beam deposited microcrystalline Si and Ge has been studied by RS, Transmission Electron Microscopy (TEM) and conductivity. It is found that RS can detect point defects not observed by TEM. Information about the electric fields in the space-charge region of heavily doped $\langle 100 \rangle$ n-GaAs has been obtained from symmetry forbidden polarization selection rules. We have performed the first comprehensive study of polished-induced strain in $\langle 100 \rangle$ and $\langle 111 \rangle$ GaAs and InP. A detailed lineshape analysis of the RS has yielded important information about surface strain, strain skin-depth and the diffusion of damage into the material.

In the second phase of our program we investigated (a) the excitation wavelength and pump chopping frequency dependence of photorefectance (PR) in $\text{Hg}_{1-x}\text{Cd}_x\text{Te}$ and (b) the properties of the $\text{Hg}_{0.7}\text{Cd}_{0.3}\text{Te}/\text{SiO}_2$ -Photox interface using photo-and bias-induced charging. The former experiment yielded information about the quality of $\text{Hg}_{1-x}\text{Cd}_x\text{Te}$ produced by various growth conditions as well as surface states. The latter work gave significant insights into the natures of traps at the $\text{Hg}_{1-x}\text{Cd}_x\text{Te}/\text{SiO}_2$ -Photox interface.

II. EXPERIMENTAL RESULTS

A. Raman Spectroscopy Study of the Effect of Growth Conditions on Alloy Potential Fluctuations in $\text{Al}_{0.48}\text{In}_{0.52}\text{As}/\text{InP}$

We have measured 300°K Raman scattering (RS) from several samples of $\langle 100 \rangle$ $\text{Al}_{0.48}\text{In}_{0.52}\text{As}/\text{InP}$ grown by molecular beam epitaxy with substrate temperatures, T_s , in the range $495^\circ\text{C} < T_s < 550^\circ\text{C}$ ¹. The 4°K photoluminescence (PL) from these samples has also been studied¹. The details of the longitudinal optic phonon RS line-shape are interpreted in terms of a "Spatial Correlation Model". At $T_s = 515^\circ\text{C}$ there is a significant decrease in both RS and PL linewidths indicating that under this growth condition there is a decrease in the alloy potential fluctuations, i.e., a tendency towards ordering. The "Spatial Correlation Model" line-shape analysis is compared with a recently proposed "Discrete-Continuum Interaction Model", i.e., Fano-type interaction.

The ternary alloy $\text{Al}_x\text{In}_{1-x}\text{As}$ is important for both fundamental and technological reasons. With regard to the former considerations this material should exhibit bond-length (and bond-angle) distortions similar to those found recently in $\text{Ga}_x\text{In}_{1-x}\text{As}$ ¹. The resultant internal strain is found to be larger for the disordered phase in relation to the ordered phase and thus may serve to stabilize the ordered phase³⁻⁵. Orderings in the systems GaAlAs ⁶, InGaAs ⁷, Ga_2AsSb ⁸ and SiGe ⁹ have recently been reported. The role of the growth temperature has been discussed by Srivastava¹⁰ et. al and Mbaye¹¹ et. al. On the basis of their first-principles total-energy and phase-diagram calculations these authors have proposed that whereas at high temperatures ($T > T_c$) such systems are stable in the disordered phase at lower temperatures ($T < T_c$) an ordered phase or clustered (pseudo-ordered) phase can become the ground state. Ichimura and Sasaki's calculation shows that there is a preference for ordering in the III-IV ternary alloys.¹² In the area of technology, devices using the $\text{Al}_{0.48}\text{In}_{0.52}\text{As}/\text{Ga}_{0.47}\text{In}_{0.53}\text{As}$ heterostructure include high-mobility modulation-doped structures¹², double-heterostructure lasers which emit at $1.55 \mu\text{m}$ ¹³, quantum well structures which show promise for lasers emitting from less than $1.3\text{-}1.65 \mu\text{m}$ ¹³, high-speed long-wavelength quantum-well avalanche photodiodes¹⁴, etc.

We have studied 300K Raman scattering (RS) measurements of a number of samples of $\langle 100 \rangle$ $\text{Al}_{0.48}\text{In}_{0.52}\text{As}/\text{InP}$ grown by MBE with substrate temperatures in the range $495^\circ\text{C} < T_s < 550^\circ\text{C}$. It should be noted that $\text{Al}_{0.48}\text{In}_{0.52}\text{As}$ is approximately AlInAs_2 . For comparison purposes we have also studied the 4K photoluminescence (PL) of these same samples. It has recently been suggested that PL¹⁵⁻¹⁸ and RS¹⁹⁻²⁰ can be used to study the microscopic alloy potential fluctuations in alloy semiconductors. There is a strong correlation between the details of the RS line-shape and the PL linewidth. At $T_s = 515^\circ\text{C}$ there is a significant decrease in both the RS and PL linewidths, indicating that under this growth condition there is a decrease in the alloy potential fluctuations, i.e., a tendency towards ordering.

The RS of this alloy system exhibits a two-mode behavior corresponding to "AlAs-like" and "InAs-like" lattice vibrations. The first order longitudinal optic (LO) phonon Raman lines exhibit a low-frequency asymmetrically broadened line-shape. We have analyzed this line-shape in terms of the "Spatial Correlation Model" (SCM)¹⁹. The line-shapes of the "AlAs-like" mode for all samples and the "InAs-like" mode for $T_s = 515^\circ\text{C}$ can be fit by the SCM using only one adjustable parameter, i.e., the "Spatial Correlation Length", ℓ ¹⁹. However, for the "InAs-like" mode for $T_s \neq 515^\circ\text{C}$ both ℓ and the intrinsic linewidth (Γ_0) must be varied to achieve a fit (two parameter fit). This indicates that for these growth conditions a new scattering mechanism has become available for this mode. The recent suggestion that a Fano model²¹⁻²² (two-parameter fit), rather than the SCM, can be used to account for the LO phonon line-shape of alloy semiconductors will be discussed.

The details of the sample growth procedures are given in Ref. 13. The AlInAs epilayers were typically 2500Å. The RS measurements were performed at 300K using the 5145Å line of an Ar-ion laser. The scattering geometry was $x(y,z)x$ where $x = \langle 100 \rangle$, $y = \langle 010 \rangle$ and $z = \langle 001 \rangle$. For this configuration only LO phonon scattering is allowed in the first-order RS. To minimize heating effects a line focus ($100\mu\text{m} \times 3\text{mm}$) was used for the laser beam (typical power of 1 watt) and the sample was thermally bonded to a heat sink.

Shown in Fig. 1 is the 300°K RS of $\text{Al}_{0.48}\text{In}_{0.52}\text{As}/\text{InP}$ sample C ($T_s = 515^\circ\text{C}$). The spectrum is typical of all the samples used in this study. The large feature at about 240 cm^{-1} is identified as the "InAs-like" LO phonon

mode and is designated LO_2 while the peak at about 365 cm^{-1} is the "AlAs-like" LO mode, labelled LO_1 . The frequencies of both these modes agree well with other results¹⁴. The weak broad structure around 180 cm^{-1} is probably related to disorder-activated zone-edge modes.

In the SCM the Raman intensity $I(\omega)$ at frequency ω is given by¹⁹:

$$I(\omega) \propto \int_{BZ} \exp(-\ell^2 q^2/4) \frac{d^3 q}{[\omega - \omega(q)]^2 + [\Gamma_0/2]^2} \quad (1)$$

where BZ denotes the Brillouin zone, ℓ is the "Spatial Correlation Length" and Γ_0 is the intrinsic linewidth of the relevant end point material. For the dispersion $\omega(q)$ of the LO phonon we take the analytical relationship based on the linear chain model:

$$\omega^2(q) = A + \{A^2 - B[1 - \cos(\pi q)]\}^{1/2} \quad (2)$$

For the "AlAs-like" modes we take $A = 8.2 \times 10^4 \text{ cm}^{-2}$ and $B = 2.23 \times 10^9 \text{ cm}^{-4}$ while for the "InAs-like" modes the parameters are $A = 2.83 \times 10^4 \text{ cm}^{-2}$ and $B = 3.4 \times 10^8 \text{ cm}^{-4}$.

Shown by the dotted lines in Fig. 2 are the experimental data for the LO_1 and LO_2 Raman bands of $Al_{0.48}In_{0.52}As/InP$ samples A, C and F. Representative error bars for the data are shown. The values of T_s for the samples used in this study are listed in Table I. To fit the "AlAs-like" modes we have used Eq. (1) and (2) with $\Gamma_{01} = 2.8 \text{ cm}^{-1}$, in good agreement with the 300K intrinsic linewidth of the end point material AlAs. The solid lines for the LO_1 modes of the three samples in Fig. 2 are a least squares fit of Eqs. (1) and (2) to the experimental data using only ℓ_1 , the "Spatial Correlation Length" of this mode, as an adjustable parameter. We refer to this as the one parameter SCM fit. The agreement between experiment and fit is quite good. Values of ℓ_1 (and Γ_{01}) for the various samples used in this study are listed in Table I.

For the "InAs-like" mode of sample C ($T_s = 515^\circ\text{C}$) the data also can be fit by the SCM using $\Gamma_{02} = 2.8 \text{ cm}^{-1}$ (intrinsic 300K linewidth of InAs) and

varying only ℓ_2 i.e., one parameter SCM fit. This is shown by the solid line in Fig. 2 for this mode, the value of ℓ_2 being listed in Table I. For the LO_2 modes of the other samples we have not been able to achieve a good fit by the one parameter SCM model. For these features we have had to vary not only ℓ_2 but also Γ_{02} . This two parameter SCM fit is shown by the dashed lines for LO_2 for samples A and F in Fig. 2. The values of Γ_{02} and ℓ_2 also are listed in Table I for the different samples. The significance of varying Γ_0 in addition to ℓ will be discussed below.

From the SCM line-shape fit we can also evaluate the full-width at half-maximum of the LO_1 and LO_2 modes, which we designate at Γ_{t1} and Γ_{t2} , respectively. These values also are listed in Table I.

For the LO_2 mode for all samples except C the parameter Γ_{02} as well as ℓ_2 had to be varied in the SCM fit (See Fig. 2). This is an indication that for these samples a new scattering mechanism has been activated by the growth conditions. The intrinsic linewidth Γ_0 of the end point materials at a given temperature is a consequence of anharmonic interactions involving two phonon processes, the most important decay channels being combinations of both optical and acoustical phonons²³. Reference 23 points out that the intrinsic phonon lifetime is related to Γ_0 through the energy-time uncertainty relationship. Thus a change in Γ_0 indicates that new energy relaxation channels have opened up.

In addition to the RS at 300°K we have also measured in PL at 4°K. Figure 3 shows the dependence of the PL linewidth on T_s . All the samples exhibited the same peak energy¹³. The values of the PL linewidth also are listed in Table I for the samples of this study. The 16 meV linewidth of sample C and the 19 meV linewidth of sample D are significantly narrower than previously reported values (~25 meV) for this material^{12,24}.

Several authors have discussed the origins of broadening in the PL of alloy semiconductors.¹⁵⁻¹⁷ Schubert et al. have investigated the effects of thermal broadening, macroscopic inhomogeneity and alloy broadening due to random cation distribution in $Ga_{1-x}Al_xAs$ ¹⁶. References 15 and 16 have presented statistical models based on this random distribution to account for the low temperature PL linewidth, the two calculations arriving at the same result. In Ref. 17 a quantum mechanical formalism was used to evaluate the exciton volume, thus leading to more realistic values of the exciton linewidth. Singh and Bajaj^{15,16} have pointed out that the linewidth is

strongly dependent on the short range disorder present in the alloy. Raman scattering provides an important complement to PL in evaluating alloy potential fluctuations. For example, the PL linewidth may also be influenced by impurities while RS line-shapes are relatively insensitive to this parameter. The LO phonon linewidth from the depletion layer of n-GaAs for $n=1 \times 10^{19} \text{ cm}^{-3}$ is essentially the same as undoped material.²⁵

The results of the RS and PL measurements clearly show that of all the material studied sample C, with $T_s = 515^\circ\text{C}$ exhibits the optimal optical properties. It has the narrowest PL and RS linewidths, has the largest ℓ_1 and in addition, has the smallest Γ_{02} (equal to that of the end point material) so that the one parameter SCM can be used to fit both LO_1 and LO_2 . Thus we conclude that under this growth condition there is a decrease in the alloy potential fluctuations of this material, i.e. a tendency towards ordering. The material $\text{Al}_{0.48}\text{In}_{0.52}\text{As}/\text{In}$ is approximately a 50-50 mixture of AlAs and InAs (AlInAs_2) and hence has the maximum bond-length and bond-angle distortions which would serve to drive the system to ordering under the proper thermodynamic conditions³⁻⁵.

It has been suggested recently that the asymmetry in the LO phonon line-shape in alloys can be accounted for by a "Discrete-Continuum Model", i.e. Fano-type interaction^{21,22}. The Fano model always involves two parameters, i.e., an asymmetry factor (Q_F) and broadening parameter (Γ_F). In Fig. 4 we have again plotted the experimental data (dotted lines) for samples A, C and F. The solid lines for both LO_1 and LO_2 are a least-squares fit of the data to Eq. (2) of Ref. 22. The fit using the Fano model is quite good and is comparable to the SCM fit in Fig. 2. The obtained values of Q_F and Γ_F for these samples is indicated in the figure. We have found that sample C has the smallest Γ_F for both modes. The main result of this comparison is to demonstrate that as far as fitting procedures are concerned the two parameter SCM model is equivalent to the two parameter Fano model. The authors of Ref. 22 have compared the Fano model to the one parameter SCM without explicitly pointing out that the former intrinsically involves two variables without considering a two parameter SCM.

B. Raman, Transmission Electron Microscopy and Conductivity Measurements of Molecular Beam Deposited Microcrystalline Si and Ge.

The structure of molecular beam deposited microcrystalline silicon and germanium films prepared under different growth conditions has been analysed by conventional transmission electron microscope (TEM) and Raman scattering (RS) and compared to electrical conductivity experiments²⁶. The TEM measurements yield an average grain size L_0 ranging from 200Å to 1.5 μm . On the other hand, the line shape of the RS is determined by a mean free path related to the average separation ℓ between defects (or impurities), where $\ell \approx 150\text{Å}$. We find in a number of cases that the electrical conductivity is determined by ℓ rather than L_0 . This experiment demonstrates the significance of RS as a structural characterization method when used in conjunction with other techniques such as TEM.

In this work, the structure of molecular beam deposited (MBD) $\mu\text{c-Si}$ and $\mu\text{c-Ge}$ films grown under different conditions has been analyzed by TEM and RS. The TEM measurements reveal that the films have an average grain size ranging from 200Å to 1.5 μm . In contrast, the line shape of the Raman spectrum (i.e., linewidth and asymmetric broadening) indicates a value of ℓ much smaller than the grain size L_0 determined by TEM. The discrepancy is attributed to generic defects or impurities introduced during growth. These defects (or impurities) destroy the translational symmetry of the crystal, reduce the mean free path of the electron-phonon system, and hence, affect the Raman line shape in a manner similar to that observed for structural damage²⁷ or finite particle size^{28,29}. We find that in our films $\ell \lesssim 150\text{Å}$ and that, in a number of cases, it dominates the electrical conductivity.

The usual $q = 0$ selection rule of first-order Raman scattering is a consequence of the full translational symmetry of an "ideal" crystal³⁰. The RS of an "ideal" diamond or zincblende type material has a Lorentzian line shape with an intrinsic linewidth of about 3 cm^{-1} at room temperature. Several authors^{28,29,31} have reported that "finite size effects" (such as those observed in $\mu\text{c-Si}$), which destroy the full translational symmetry of the material, result in a low-frequency asymmetric broadening and red shift of the Raman spectra; however, other physical phenomena which also destroy the translational symmetry of the system, such as structural damage,²⁷ alloying,¹⁹ etc., produce a similar "q-vector relaxation" of the RS. From the details of the RS line shape a parameter can be determined which is a measure

of the average distance between defects (structural damage) or finite particle size ($\mu\text{c-Si}$). In our experiments on $\mu\text{c-Si}$ and $\mu\text{c-Ge}$, the RS line shape is determined by the mean free path of the electron-phonon system induced by defects (or impurities) rather than the particle size effect. On this basis, we cannot only explain why the determined by RS is much smaller than the grain size L_0 evaluated by TEM, but can arrive at a quantitative measure of the mean free path. In general, when the mean free path is comparable to the particle size L_0 , the fit is further complicated by the Matthiessen's rule,³² where $L^{-1} = \ell^{-1} + L_0^{-1}$; however, in most of our present work, $\ell < L_0$, thus, the Raman spectra are mainly influenced by ℓ .

It has been shown that the details of the Raman line shape (i.e., shift and asymmetry) associated with q-vector relaxation can be accounted for by a model which assumes a Gaussian spatial correlation.^{27,28} In this letter, we extend this model to take into account the finite instrumental resolution of the Raman system in order to make a more accurate comparison with experiment. If we assume an isotropic, the Raman intensity at frequency ω , $I(\omega)$, can be written as

$$I(\omega) \propto \int_0^1 d^3q \exp(-q^2 \ell^2/4) \int_{-\infty}^{\infty} \frac{(\Gamma_0/2\pi) T(\epsilon) d\epsilon}{[\omega - \omega(q) - \epsilon]^2 + [\Gamma_0/2]^2} \quad (3)$$

where q is expressed in units of $2\pi/a$, a being the lattice constant, and $\Gamma_0 = 3.0 \text{ cm}^{-1}$ is the intrinsic Raman linewidth at 300K. For simplicity, we assume a triangular instrumental transfer function (the integral having a very simple analytical form³³) with a full width at half-maximum $\Gamma_1 (= 1 \text{ cm}^{-1}$ for our experimental conditions). For the dispersion $\omega(q)$, we have used an analytical form for a one-dimensional linear chain model as in Eq. (2). From the above equation, the full width at half-maximum $\Gamma (= \Gamma_a + \Gamma_b)$ and asymmetry (Γ_a/Γ_b) can be determined as a function of ℓ , where Γ_a and Γ_b are the low and high frequency half-widths, respectively. This equation differs from Eq. (1) since it explicitly includes the instrumental transfer function $T(\epsilon)$. Thus it is more complete than Eq. (1).

Shown by the solid line in Figs. 5(a) and 5(b) are Γ and Γ_a/Γ_b as a function of ℓ for the case of Si and Ge, respectively, evaluated from

Eq. (3). Also shown are the experimental values of Γ and Γ_a/Γ_b obtained from samples prepared under various deposition conditions. A more detailed description of sample preparation can be found in Ref. 34. As can be seen, the agreement between experimental and calculated Γ and Γ_a/Γ_b values for Si and Ge is quite good. Notice that for all the measured Si and Ge samples, $\ell \lesssim 150\text{\AA}$.

Figure 6 shows the TEM micrograph for a germanium film having a thickness of approximately 1000\AA . The film was deposited at a substrate temperature $T_s = 180^\circ\text{C}$ followed by thermal annealing at 550°C for 1 h. From Fig. 6(b) it is clear that that average grain size exceeds $1\mu\text{m}$. In Fig. 6(a) the nearly single crystalline electron diffraction patterns further indicate that the microcrystalline grain size exceeds the electron beam size; however, Raman measurements in the same sample show that the optical phonon branch has a full width at half-maximum of 4.5cm^{-1} and an asymmetry of 1.25. According to Fig. 5(b), this corresponds to $\ell \approx 150\text{\AA}$.

The comparison of these two experimental results shows that while TEM reveals the dimensions of the grain structure, RS can be used to infer the presence of local structural defects through a parameter dictated by ℓ . Obviously, the detailed microscopic description of these structural defects is not embodied in our approach.

Figures 7 and 8 compare room-temperature electrical conductivity and Raman linewidth Γ measurements for $\mu\text{c-Si}$ and $\mu\text{c-Ge}$ films, respectively, as a function of isochronal anneals. The data points were obtained from samples prepared at various T_s . For silicon, the anneals are in the range of $600\text{--}800^\circ\text{C}$ while for germanium the range varies from 400 to 550°C ; in the latter material the lower range was used since crystallization in germanium occurs at lower temperatures compared to Si films.

For the as-prepared silicon samples, $T_s < 360^\circ\text{C}$ leads to totally amorphous structures, at 380 to 420°C a mixed phase of amorphous and crystalline material was observed, whereas for $T_s > 420^\circ\text{C}$ a complete microcrystalline structure is obtained. The corresponding temperatures for germanium are $T_s < 180^\circ\text{C}$, $180^\circ\text{C} < T_s < 200^\circ\text{C}$, and $T_s > 220^\circ\text{C}$, respectively. In addition, the transition from amorphous to crystalline phase in as-deposited amorphous silicon films was observed at annealing temperatures $T_a > 600^\circ\text{C}$ for one hour depending on the preparation conditions. For amorphous germanium heat treatments at $T_a > 450^\circ\text{C}$ lead to microcrystalline samples.

Indicated in Figs. 7 and 8 is the average particle size (L_0) as determined by TEM analysis after the annealing 800 and 550°C respectively; however, no appreciable change in L_0 was observed for lower annealing temperatures as long as no amorphous component was present prior to the annealing. Notice that the values for L_0 range from 200Å to 1.5 μm depending on T_s . Tsu et al.³⁴ have previously used a quantitative model based on homogeneous and impurity induced heterogeneous nucleation to explain the wide range in particle size observed in MBD-prepared $\mu\text{c-Si}$ and $\mu\text{c-Ge}$. They found that the presence of impurities in the as-prepared amorphous films, particularly at lower T_s , results in smaller particles upon crystallization. The top parts of Figs. 7 and 8 show σ for Si and Ge films respectively as a function of the annealing temperature. For Si, after annealing at 800°C, a total increase in σ of approximately two orders of magnitude was observed for samples having $L_0 \sim 1.5\mu\text{m}$. The total increase in conductivity gradually decreases as the average particle size L_0 decreases. In samples prepared either at $T_s > 600^\circ\text{C}$ or at $T_s < 200^\circ\text{C}$ no significant change in σ was observed. The increase in σ for intermediate T_s is attributed to the annealing of some of the structural defects introduced during the crystallization process occurring at lower temperatures. Raman measurements [Fig. 7(b)] on the same samples after each annealing step correlate well with conductivity measurements. For intermediate T_s , the Raman linewidth Γ decreases as T_a is increased. According to Fig. 5(a), the decrease in Γ corresponds to an increase in the length l . The similar trend of σ and l indicates a reduction in the defect density after annealing.

Previously we found that the void structure of MBD-prepared silicon films deposited at $T_s > 350^\circ\text{C}$ is much reduced, therefore limiting the indiffusion of impurities. Thus, we believe that the increase in both σ and l is related to defects rather than impurities. At high deposition temperature, for instance, $T_s = 600^\circ\text{C}$ in Fig. 7, the structural defects are annealed during the growth process and therefore no change in either conductivity or Raman linewidth is observed for post-deposition heat treatments. The situation is quite different for samples having small particles. At $T_s = 200^\circ\text{C}$, the particle size is in the range of 200Å as determined by TEM. Heat treatments do not change significantly either the electrical conductivity or the Raman linewidth. What this suggests is that, unlike samples having

larger particle size, the dominant scattering mechanism is due to grain boundaries.

For Ge, in the range of annealing temperatures used as shown in Figs. 8(a) and 8(b), no appreciable change in either σ or Γ was observed. This may be due to the fact that there are fewer generic defects present in Ge as compared to Si although another possibility is that the structural defects in germanium are more stable than in silicon and perhaps annealing temperatures in excess of 550°C are needed to observe the thermal annealing of the defects.

C. Symmetry Forbidden LO-phonon Raman Scattering from Electric Fields in the Space Charge Region in Heavily Doped <100> n-GaAs.

We have investigated symmetry forbidden longitudinal optic Raman scattering for various polarization configurations at 4579 Å from the <100> surface of heavily doped n-GaAs caused by the strong surface-fields and high impurity levels³⁵. We have evaluated the magnitude and phase of the coefficient of the electric-field induced term as well as the magnitude of the coefficient of the impurity-induced factor. These parameters can be used to gain information about the surface electric fields in <100> n-GaAs.

We have studied the symmetry forbidden LO phonon RS from the <100> surface of heavily doped n-GaAs:Si due to the high impurity levels and strong surface electric fields. The samples were grown by molecular beam epitaxy and had free carrier concentration (electrons) in the range $1 \times 10^{18} \text{ cm}^{-3}$ to $1 \times 10^{19} \text{ cm}^{-3}$. The free carrier concentration as well as space charge region (SCR) electric-fields have been well characterized in previous studies^{36,37}. The measurements were made at room temperature in the backscattering geometry using the 4579 Å line of an Ar-ion laser. We have studied RS for all four possible polarization configurations, i.e., $I_1[x(y,z)\bar{x}]$, $I_2[x(y,y)\bar{x}]$, $I_3[x(y',y')\bar{x}]$, and $I_4[x(z',z')\bar{x}]$, where $x = \langle 100 \rangle$, $y = \langle 010 \rangle$, $z = \langle 001 \rangle$, $y' = \langle 011 \rangle$ and $z' = \langle 0\bar{1}1 \rangle$. From these measurements we have evaluated the coefficients of the electric field- and impurity-induced terms at 4579 Å.

Shown in Figure 9 is the RS from sample 782-8A in the normally allowed configuration $I_1[x(y,z)\bar{x}]$. The peaks designated L_+ and L_- are the coupled plasmon -LO phonon modes which originate from the bulk of the material where the free carriers exist. The structure marked LO (292 cm^{-1}) is the

unscreened LO phonon mode of GaAs which originates only from the SCR. In previous studies the L_+ , L_- modes have been used to characterize the free carrier concentration^{36,37} (and hence impurity concentration). Since GaAs is degenerate for $n > 1 \times 10^{18} \text{ cm}^{-3}$ we take the impurity concentration, n_i , equal to the free carrier concentration, n . The amplitude of LO(292 cm^{-1}), in relation to that of an undoped sample, has been utilized to evaluate the width of the SCR and hence the built-in surface electric field³⁶. In this study we will concentrate on the polarization dependence of the unscreened LO (292 cm^{-1}) mode.

In Fig. 10 we display, by the points, the experimentally determined ratios I_2/I_1 , I_3/I_1 and I_4/I_1 as a function of impurity concentration n_i for a laser excitation wavelength of 4579Å. Note that as $n_i \rightarrow 0$, the ratio $I_2/I_1 \rightarrow 0$ while both I_3/I_1 and $I_4/I_1 \rightarrow 1$. We will show below that difference between I_3/I_1 and I_4/I_1 with increasing n_i is due to an interference effect similar to that reported in Refs. 38 and 39.

The effects of electric fields and linear-q terms on the Raman tensor have been discussed in several articles^{40,41}. We will demonstrate below that linear-q terms are not significant in our experiment and hence we will consider only the electric field-induced effects. Impurity-induced terms will be discussed in the next paragraph. For the case of LO-phonon scattering from $\langle 100 \rangle$, with the electric field $\mathcal{E}(x)$ also along this crystallographic direction, the Raman tensor can be written as^{40,41}:

$$\begin{pmatrix} a_1 e^{i\phi_1} \mathcal{E}(x) & 0 & 0 \\ 0 & a_2 e^{i\phi_2} \mathcal{E}(x) & d e^{i\phi_3} \\ 0 & d e^{i\phi_3} & a_2 e^{i\phi_2} \mathcal{E}(x) \end{pmatrix} \quad (4)$$

In Eq. (4) a_1 (a_2) and ϕ_1 (ϕ_2) are the magnitude and phase, respectively, of the electric field-induced term while d and ϕ_3 are related to the normally allowed atomic-deformation (AD) scattering process. For our scattering geometry, i.e., from the $\langle 100 \rangle$ surface, it can be shown from Eq. (4) that only a_2 , ϕ_2 , d , and ϕ_3 can be observed.

The Raman tensor for impurity-induced scattering can be written as^{38,39}:

$$\begin{pmatrix} 1 & 0 & 0 \\ 0 & 1 & 0 \\ 0 & 0 & 1 \end{pmatrix} C n_i^{1/2} \exp(i\phi_4) \quad (5)$$

where C and ϕ_4 are the magnitude and phase, respectively, of the coefficient for this process. It has been demonstrated by Menendez and Cardona that Eqs. (4) and (5) represent independent scattering processes^{38,39}. Therefore, in order to calculate the total scattering intensity the two processes must be added after squaring, not before squaring.

From Eqs. (4) and (5) we can write expressions for the ratios of the intensities of the various polarization configurations:

$$I_2/I_1 = \frac{\int_0^{L_s} [a_2^2 \varepsilon^2(x) + c^2 n_i] e^{-2\alpha(\lambda)x} dx}{\int_0^{L_s} d^2 e^{-2\alpha(\lambda)x} dx} \quad (6a)$$

$$I_3/I_1 = \frac{\int_0^{L_s} \{ |a_2 e^{i\phi} \varepsilon(x) - d|^2 + c^2 n_i \} e^{-2\alpha(\lambda)x} dx}{\int_0^{L_s} d^2 e^{-2\alpha(\lambda)x} dx} \quad (6b)$$

$$I_4/I_1 = \frac{\int_0^{L_s} \{ |a_2 e^{i\phi} + d|^2 + c^2 n_i \} e^{-2\alpha(\lambda)x} dx}{\int_0^{L_s} d^2 e^{-2\alpha(\lambda)x} dx} \quad (6c)$$

where $\phi = (\phi_2 - \phi_3)$, L_S is the width of the depletion region and $\alpha(\lambda)$ is the penetration depth of the light at wavelength λ , respectively. In Eqs. (6) we have neglected the small difference in wavelength between the incident and scattered light. Expressions for L_S and $\mathcal{E}(x)$ as a function of n_i are given in Ref. 36. The quantity $\alpha(\lambda)$ is obtained from the work of Aspnes and Studna⁴². Note that Eqs. (6b) and (6c) exhibit an interference between the electric-field-induced and AD terms similar to that discussed in Refs. 38 and 39.

The solid lines in Fig. 10 are at least squares fit of Eqs. (6) to the experimental points. From such an analysis we can evaluate

$$\begin{aligned} a_2/d &= (5.0 \pm 1.0) \times 10^{-7} \text{ cm/V} \\ \phi &= 60 \pm 10^\circ \\ C^2/d^2 &= (1.4 \pm 0.2) \times 10^{-20} \text{ cm}^3 \end{aligned}$$

Grimsditch et al⁴³ have measured d and also have derived a theoretical expression from which both d and ϕ_3 can be evaluated as a function of λ . For 4679A both experiment and theory yield $d = 200\text{\AA}^2$ while $\phi_3 = -2^\circ$ is obtained from theory. Thus we have that:

$$\begin{aligned} a_2 &= (9.6 \pm 0.4) \times 10^{-5} \text{ cm-A}^2/\text{V} \\ \phi_2 &= 62 \pm 10^\circ \\ C^2 &= (5.6 \pm 0.8) \times 10^{-16} \text{ cm}^3 \text{-A}^4 \end{aligned}$$

It has been shown that forbidden LO-scattering induced by an electric field can be written as:⁴⁴

$$a_2 e^{i\phi_2} \frac{\partial^3}{\partial \omega^3} [\omega^2 \chi_{ij}(\omega)] \quad (7)$$

where $\hbar\omega$ is the photon energy and $\chi_{ij}(\omega)$ is the linear susceptibility. In our case we are at an energy near the E_1 optical transition of GaAs. Trommer et al⁴⁵ have used a two-dimensional critical point model for the E_1 transitions so that

$$\partial^3/\partial \omega^3 [\omega^2 \chi_{ij}(\omega)] = (\omega - \omega_1 - i\eta)^{-3} \quad (8)$$

where $\hbar\omega_1$ is the energy of the E_1 transition in GaAs (-2.89 eV) and η is a broadening parameter taken to be 70 meV. Thus, from Eqs. (7) and (8) we can calculate ϕ_2 at 4579A (=2.71 eV) to be

$$\phi_2 (4579 \text{ A}) = 64^\circ$$

This value of ϕ_2 is in good agreement with our experimental value of $62 \pm 10^\circ$.

Trommer et al⁴³ have evaluated $a_2/d = 1.2 \times 10^{-16} \text{ cm/V}$ at 4416A (2.81 eV). From Ref. 43 $d = 280 \text{ \AA}^2$ and hence we can deduce that $a_2 (4416\text{A}) = 3.4 \times 10^{-4} \text{ cm-A}^2/\text{V}$. From Eqs. (7) and (8) we can determine that the ratio $a_2 (4416\text{A})/a_2(4579\text{A})=6$, in reasonable agreement with the experimental ratios of $(3.4 \times 10^{-4}/9.6 \times 10^{-5})=3.5$.

Comparison of the quantity C with other experiments is somewhat more difficult. From Ref. 39 C^2 can be evaluated⁴⁶ to be $1.4 \times 10^{-12} \text{ cm}^{-3}\text{-A}^4$ at 1.85 eV. This value is considerably larger than that obtained from our experiment, i.e. $5.6 \times 10^{-16} \text{ cm}^{-3}\text{-A}^4$. This is not too surprising since $C^2(\omega)$ has maxima under resonance conditions and the value of Ref. 8 was deduced from resonance with the $E_0 + \Delta_0$ optical transition.

We have neglected linear- q terms based on the results of a study of the Raman spectra of $\langle 100 \rangle$ GaAs implanted with various fluences of As-ions²⁷. It was found that the highest fluences produced an undamaged region of dimensions 45-50A but that no violation of the polarization selection rules for this fluence was observed. Therefore, we conclude that for dimensions of the order finite size effects, i.e., linear - q terms are not significant.

For $n_i \approx 1 \times 10^{19} \text{ cm}^{-3}$, the highest impurity level used in this study, the width of the SCR is about 50 \AA ³⁶. Therefore, we have neglected linear -q terms in our analysis.

D. Comprehensive Investigation of Polish-Induced Surface Strain in $\langle 100 \rangle$ and $\langle 111 \rangle$ GaAs and InP

We have performed a systematic and extensive investigation of polish-induced surface strain in $\langle 100 \rangle$ and $\langle 111 \rangle$ GaAs and InP using Raman scattering from the Longitudinal optical (LO) phonon modes⁴⁷⁻⁴⁹. By using various lines of an Ar-ion laser it was possible to accomplish non-destructive depth profiling⁴⁷⁻⁴⁹. To account for the observed lineshape changes we have used a mode which is based on the convolution of the penetration depth of the light and skin depth of the polish-induced surface strain. From such an analysis, we have obtained the polish induced surface strain, skin depth of the strain and inhomogeneous broadening. For the $\langle 100 \rangle$ surface, the strain is about 2-3% in both materials and the skin depth (100-500 Å) is relatively independent of particle size. In contrast, for the $\langle 111 \rangle$ surface, the average surface strain is only about 0.6% for GaAs and 1.2% for InP and the skin depth is of the order the particle size. The dependence of the strain skin depth on polish time also has been studied. A qualitative argument based on polish-induced bond breaking is proposed to explain why surface strain for $\langle 111 \rangle$ is considerably less than for $\langle 100 \rangle$ and why the strain is compressive for both surfaces. Using a one dimensional diffusion model, we can successfully explain the depth-dependence of the polish-induced strain and the polish time dependence of the damage skin-depth. This analysis yields a diffusion coefficient for the polish-induced strain for the two surfaces. Our diffusion model is consistent with the conventional model of chemo-mechanical polishing of compound semiconductor.

Polish-induced surface damage⁵⁰ in diamond and zincblende-type semiconductors has been investigated by several methods including optical techniques such as photoluminescence⁵¹, reflectance⁵²⁻⁵⁴, absorption⁵⁵, photon backscattering⁵⁶, double crystal X-ray diffractometry⁵⁷, transmission electron microscopy (TEM)⁵⁷, and Raman spectroscopy (RS)⁵⁷⁻⁵⁹. The technique of RS is extremely useful for a number of reasons. The influence on the RS spectrum of damage-induced perturbations such as strain^{40,60} and

disorder²⁷ (which produce different effects) are well understood. Nondestructive depth profiling can be done using various laser lines. Since the Longitudinal Optical (LO) phonon in zincblende-type materials is a singlet, certain complications which occur in electronic transition spectroscopies are avoided such as strain-induced interband and intraband splitting⁶¹.

1. Measurement Conditions

The method of preparation of the samples is described in Ref. 47. All measurements were made at room temperature, using an Ar-ion laser as an excitation source with output wavelengths at 5145, 5017, 4880, 4765, and 4579 Å. In order to avoid heating effects a line focus (300 μm \times 3 mm) was used in which the power was 300 mW (except for 4579 and 5017 Å, in which case it was 130 mW). For the $\langle 100 \rangle$ surface, the allowed cross polarization configuration $[x(y,z)x]$ was employed to reduce the Rayleigh scattering from the rough surface, where x, y, z indicate $\langle 100 \rangle$, $\langle 010 \rangle$, and $\langle 001 \rangle$, respectively. The cross configuration for the $\langle 111 \rangle$ surface is forbidden so it was not analyzed. We found no significant difference in the line shape for different polarizations.

2. $\langle 100 \rangle$ Surface

Shown in the Fig. 11(a) is the RS using the 5145 Å line (labeled A) in the region of LO phonon for undamaged $\langle 100 \rangle$ InP and material polished with 0.05 μm grit for the three different times (5, 10, and 60 minutes). The undamaged RS is fairly sharp, with a symmetry peak center at 345.6 cm^{-1} . Spectrum B, for which the polishing time is 5 minutes, has a relatively sharp feature at about 348 cm^{-1} and a broad shoulder at about 355 cm^{-1} . As the polish time increases, the amplitude of the shoulder grows relative to the low frequency feature, but the position of the shoulder does not shift.

The spectra in Fig. 11(b) are the results for $\langle 100 \rangle$ GaAs. Spectrum A is for undamaged material taken with a 5145 Å line, and spectra B-D are for the case of 0.05 μm grit polish for three different times (5, 10, 60 minutes, respectively). The undamaged spectrum has a sharp peak at 292.1 cm^{-1} . We see that with increasing polish time, the amplitude of the shoulder grows relative to the low-frequency feature, and the position of the shoulder shifts to higher frequencies. We will demonstrate later in the paper that the two features in the spectra of damaged InP and GaAs do not arise from

two separate peaks but are the consequence of the convolution of the skin depth of the damage-induced strain and the optical penetration depth for the various wavelengths.

Plotted in Fig. 12 are the results for $\langle 100 \rangle$ InP and GaAs for fixed time and different wavelengths. The InP was polished with 0.05 μm grit for 5 minutes as shown in Fig. 12(a), while GaAs was polished with 0.3 μm grit for 60 minutes as shown in Fig 12(b). The spectra were taken with 5145, 5017, 4880, 4765 and 4579 A excitation lines, respectively, for both materials. The amplitude of RS of the damaged material was considerably less than the undamaged sample although the integrated intensities remained approximately constant. We can see that as the penetration depth of the light decreases, the amplitude of the high frequency shoulder grows relative to the low frequency feature. For GaAs the high-frequency shoulder in spectrum B has become the dominant feature at the shortest wavelength.

3. $\langle 111 \rangle$ Surface

Plotted in Fig 13(a) are the RS in the region of the LO phonon for undamaged $\langle 111 \rangle$ InP using the 5145-A line (spectrum A) and polished with 0.05 μm grit for 10 minutes using 5145, 4880, and 4579 A excitation lines (labeled B, C, and D ,respectively). We have not plotted the spectra for all wavelengths since there are no significant differences between them. The $\langle 111 \rangle$ and $\langle 100 \rangle$ [see Fig. 12(a)] undamaged RS are identical in terms of peak position and linewidth. However, for damaged conditions, the RS from the $\langle 111 \rangle$ surface are quite different from those from the $\langle 100 \rangle$ surface. The relatively sharp feature at about 348 cm^{-1} , which appeared in the RS from the $\langle 100 \rangle$ surface [see Fig 12(a)], is not seen. The broadening is fairly symmetrical, and spectra peak at about $346.5\text{--}347.5\text{ cm}^{-1}$. As the penetration depth of the light decreases, the linewidth increases and the peak position shifts to the blue.

The RS spectra in the region of the LO phonon for undamaged and damaged $\langle 111 \rangle$ GaAs, polished with 0.3 μm grit for 10 minutes, are shown in Fig 3(b).As for case of InP, the undamaged spectra for $\langle 111 \rangle$ and $\langle 100 \rangle$ surfaces are identical. Also for GaAs the damaged spectra are symmetrically broadened; with decreasing wavelength the RS features broaden and shift to the blue, although not as much as for InP [see Fig 13 (a)].

The measured RS shift and line-width of the $\langle 111 \rangle$ InP and GaAs for various polishing conditions versus different penetration depths $d_o(\lambda)$ ⁴² of the different Ar-ion laser wavelengths (λ) are plotted in Fig. 14(a) and 14(b), respectively. The RS shift and linewidth for $\langle 111 \rangle$ InP and GaAs damaged with 0.3 μ m grit for 60 minutes do not change with different d_o . However, for the 0.05 μ m grit size the RS shift and linewidth do increase considerably with decreasing light penetration depth. For the undamaged surfaces, the RS shift and linewidth are constant with d_o , demonstrating that a strain-free surface can be achieved by proper mechanical and chemical polishing.

4. Analysis

a. Convolution Model

It is well known that polishing induces strain at the surface of a material thus producing a shift in LO frequency from its unstrained value^{40,47-49,60}. The damaged-induced strain (and hence RS shift) diminishes as a function of depth from the surface. The observed RS signal is the convolution of the depth dependence of the LO frequency and the optical skin depth (d_o) of the light. Assuming an exponential depth dependence for the Raman frequency:⁴⁷

$$\omega(x) = \omega_o + \Delta\omega_o \exp(-x/d_s) \quad (9)$$

$$\omega(x) = \Delta\omega_o \exp(-x/d_s) \quad (10)$$

where x is the distance from the surface, ω_o is the unperturbed frequency, $\Delta\omega_o$ is the shift due to surface strain and d_s is the skin depth of the strain. The Raman intensity $I(\omega)$ is given by

$$I(\omega) \propto \int_0^{\infty} dx L[\omega - \omega(x)] \exp(-2x/d_o) \quad (11)$$

where $L(\omega)$ is a line shape factor which is a convolution of the lorentzian line shape of the RS and the instrumental transfer function. We have neglected the small difference in the optical skin depth for the incident and scattered radiation in the above discussion. After changing variables we write:

$$\omega(\gamma) = \omega_0 + \Delta\omega_0 \gamma \quad (12)$$

where $\gamma = \exp(-x/d_s)$. Equation (11) then becomes:

$$I(\omega) \propto \int_0^\infty d\gamma L[\omega - \omega(\gamma)] \gamma^{\beta-1} \quad (13)$$

where $\beta = 2d_s/d_0$. For simplicity we have assume a triangular instrumental transfer function $T(\xi)$ with full width at half maximum of Γ_I . The quantity $L(\omega)$ can be written as:

$$L(\omega) = \int_{-\infty}^{\infty} \frac{(\Gamma/2\pi)}{(\omega - \xi)^2 + (\Gamma/2)^2} T(\xi) d\xi \quad (14)$$

where Γ is the linewidth of the RS. Equation (14) can be solved to yield the analytical form

$$L(\omega) = (\Gamma/2\pi\Gamma_I) [R(\omega + \Gamma_I) + R(\omega - \Gamma_I) - 2R(\omega)] \quad (15)$$

where

$$R(\omega) = (2\omega/\Gamma) \arctan(2\omega/\Gamma) - (1/2) \ln[(2\omega/\Gamma)^2 + 1] \quad (16)$$

After integration by parts we obtain:

$$I(\omega) \propto I_1 + I_2 + I_3 \quad (17)$$

where

$$I_1 = R(\Phi + \Gamma_I) + R(\Phi - \Gamma_I) - 2R(\Phi) \quad (18a)$$

$$\Phi = \omega - (\omega_0 + \Delta\omega_0) \quad (18b)$$

$$I_2 = A \{ \arctan[2(\Phi + \Gamma_I)/\Gamma] + \arctan[2(\Phi - \Gamma_I)/\Gamma] - 2\arctan(2\Phi/\Gamma) \} \quad (18c)$$

with

$$A = 2\Delta\omega_0/\Gamma(\beta+1) \quad (19a)$$

$$I_3 = B \int_0^{\beta+1} dy \gamma^{\beta+1} \{1/[1+(\delta+\sigma)^2] + 1/[1+(\delta-\sigma)^2] - 2/(1+\delta^2)\} \quad (19b)$$

$$B = 4(\Delta\omega_0)^2 / \Gamma^2 (\beta+1) \quad (20a)$$

$$S = 2[\omega - (\omega_0 + \Delta\omega_0 \gamma)] / \Gamma \quad (20b)$$

$$\sigma = 2\Gamma_I / \Gamma \quad (20c)$$

It is also possible to consider any inhomogeneous strain in the plane perpendicular to the polishing direction (for a given value of depth). By increasing the broadening parameter Γ in Eq.(14) from its intrinsic value Γ_0 (2.4 cm^{-1} for GaAs and 1.2 cm^{-1} for InP) and assuming a depth dependence similar to that of the frequency shift [see Eq.(9)], we can write:

$$\Gamma = \Gamma_0 + \Delta\Gamma_0 \exp(-x/d_s) \quad (21)$$

where Γ_0 is considered to be the inhomogeneous broadening.

Two dimensional strain in the plane perpendicular to the polishing direction is assumed in order to correlate the RS shift $\Delta\omega_0$ with the surface strain. The quantity $\Delta\omega_0$ for $\langle 100 \rangle$ or $\langle 111 \rangle$ surface is related to the surface strain, S , by:

$$(\Delta\omega_0/\omega_0)_{100} = [(q/\omega_0^2) - \lambda_{100}(p/\omega_0^2)] S = K_{100} S \quad (22a)$$

where

$$\lambda_{100} = C_{12}/C_{11} \quad (22b)$$

and

$$(\Delta\omega_0/\omega_0)_{111} = \{[(p+2q)(2-\lambda_{111})6\omega_0^2] - [2r(1+\lambda_{111})/3\omega_0^2]\} S = K_{111} S \quad (22c)$$

where

$$\lambda_{111} = 2(C_{11} + 2C_{12} - 2C_{44}) / (C_{11} + C_{12} + 4C_{44}) \quad (22d)$$

In the above equations, C_{11} , C_{12} , and C_{44} are elastic stiffness constants and p , q , and r are coefficients which describe the strain-induced shift of the optical phonons. For GaAs $K_{100} = -1.5$ and $K_{111} = -0.7$ ⁴⁰. The parameters p , q , and r have not been determined for InP; but since these parameters do not vary much for the III-V materials⁴⁰, we use GaAs values for InP and hence $K_{100} = -1.3$ and $K_{111} = -0.8$ for this semiconductor.

b. Fitting of <100> Surface Results

Shown in Fig 15(a) is a least-square fit of Eq(9)-(20) to the spectra at 5145 Å and 4880 Å of <100> InP damage with 0.3 µm grit for 10min. The adjustable parameters were $\Delta\omega_o$ (RS shift due to surface strain) and d_s . We have taken $\omega_o = 345.6 \text{ cm}^{-1}$ and $\Gamma_o = 1.2 \text{ cm}^{-1}$; $\Gamma_I = 2.4 \text{ cm}^{-1}$ from slit settings. The d_o value is from Ref. 42. There is excellent agreement between theory and experiment at both 5145 and 4880 Å wavelengths. We find that $\Delta\omega_o = 12.3 \text{ cm}^{-1}$ and $d_s = 386 \text{ Å}$ for 5145 Å and $\Delta\omega_o = 12.3 \text{ cm}^{-1}$ and $d_s = 380 \text{ Å}$ for 4880 Å. Listed in Table II are summaries of the results for InP (averaged over the different wavelengths) for the various conditions.

In Fig. 15(b) are plotted experiment and fit for <100> GaAs at 5145 Å and 4880 Å damaged with 0.3 µm grit for 10 mins using $\omega_o = 292.1 \text{ cm}^{-1}$, $\Gamma_o = 2.4 \text{ cm}^{-1}$, and $\Gamma_I = 2.4 \text{ cm}^{-1}$. It is found that $\Delta\omega_o = 10.7 \text{ cm}^{-1}$ and $d_s = 235 \text{ Å}$ for 5145 Å and $\Delta\omega_o = 10.9 \text{ cm}^{-1}$ and $d_s = 240 \text{ Å}$ for 4880 Å. The data for <100> GaAs for different polishing conditions are listed in Table II.

An inhomogeneous strain for <100> for both GaAs and InP was also introduced. We find that increasing $\Delta\Gamma_o$ to 3 cm^{-1} had little effect on the quality of the fits in Figs. 15(a) and 15(b); further increases, however, result in a significant deviation in the correlation between fit and experiment. Therefore, we conclude that the inhomogeneous strain is less than 3 cm^{-1} for the <100> situation. It is significantly less than the homogeneous shift, $\Delta\omega_o$, which is $8\text{-}12 \text{ cm}^{-1}$ (see Table II).

For the case of 0.05 µm grit we have performed a systematic study of the effect of the polishing time, t , on $\Delta\omega_o$ as shown in Table II. Note that while $\Delta\omega_o$ and $\Delta\omega_o$ are almost independent of polishing time (greater than 2.5 minutes) the quantity d_s saturates with increasing t . Plotted in Fig.16 by the open circles are the experimental values of d_s as a function of t for <100> polishing.

c. Fitting of $\langle 111 \rangle$ Surface Results

The interpretation of the experimental results for the $\langle 111 \rangle$ case are somewhat different from that for the $\langle 100 \rangle$ situation. We were not able to obtain a good fit to the experimental data if we used only Eq.(17), i.e. no homogeneous broadening. Therefore it was necessary to use Eq(9). For this case inhomogeneous broadening is an important effect, as found in the previous RS study⁵⁸. In contrast to the $\langle 100 \rangle$ case it is difficult to get meaningful data from the spectrum at just a single wavelength since variations in d_s and Γ produce similar effects on the theoretical fit. Therefore we have obtained values of $\Delta\omega_o$, $\Delta\Gamma_o$ and d_s for the different polishing conditions by performing a self-consistent least squares fit of Eqs(1)-(11) to all five spectra at different wavelengths, i.e., 5145, 4965, 4880, 4765, and 4579 Å. The resultant numbers are listed in Table III.

Comparing Tables II and III, we find that for the $\langle 111 \rangle$ surface, the compressive surface strain is less than that in the $\langle 100 \rangle$ case, the dominant strain is inhomogeneous, and the depth of damage-induced strain is much deeper than that of the $\langle 100 \rangle$ surface for corresponding polishing conditions.

For this surface also we have performed a systematic study of the effects of polishing time on $\Delta\omega$, $\Delta\Gamma_o$ and d_s for 0.05 μ m grit. As for the $\langle 100 \rangle$ case $\Delta\omega_o$, $\Delta\Gamma_o$ are independent of t (for $t > 2.5$ minutes) while d_s is a function of t (see Table III). The dependence of d_s on t for the case of the $\langle 111 \rangle$ surface and 0.05 μ m grit is illustrated in Fig. 17 by the open circles.

5. Discussion

Our results show that the surface strain is compressive and is about 2.2% for $\langle 100 \rangle$ GaAs, 2.6% for $\langle 100 \rangle$ InP, 0.6% for $\langle 111 \rangle$ GaAs and 1.2% for $\langle 111 \rangle$ InP. This was found from the sign and magnitude of $\Delta\omega_o$ in Tables II and III and Eqs.(11) and (12). The inhomogeneous strain ($\Delta\Gamma_o/2$) is less than 0.3% for the $\langle 100 \rangle$ surface while it is about 1.4% for the $\langle 111 \rangle$ surface. The strain skin depth is dependent on polish time and it approaches a limiting value for a long time polish with a given grit size.

We propose an ideal spring model to qualitatively account for the compressive nature of $\Delta\omega_o$ and the difference in $\Delta\omega_o$ between the two

surfaces. In addition, in order to explain the saturation and time dependence of d_s , we propose a model based on one dimensional diffusion of the strain.

We also considered the effect on the LO phonon line shape of other perturbations such as disorder, temperature gradient effects and free carrier interactions (coupled plasmon-LO modes). a. Ideal Spring Model

Shown in Figs. 18 and 19 are the zincblende crystal structure in the $\langle 100 \rangle$ and $\langle 111 \rangle$ directions, respectively. For the former case we display six layers, from n to $n+5$, while for the latter situation eight layers are shown, from n to $n+7$. The plane designated n in both figures is not necessarily the top plane, there being $n-1$ layers above it. The bond distance is $(\sqrt{3}/4) a$, where a is the lattice constant. In discussion below we assume that the bonds between atoms are ideal springs and that the effect of the polishing is to break the bonds between two given sets of layers shown in these figures.

For the $\langle 100 \rangle$ case all layer are equivalent, the atoms between each successive plane being connected by two bonds. We assume that the polishing remove all the layers above $n+1$, i.e. the bonds between n and $n+1$ are broken. The layer $n+1$ will then be pulled toward the $n+2$ plane. If this displacement is complete, i. e., the $n+1$ layer is pulled entirely into the $n+2$ plane, the bond distance between $n+1$ layer atoms and $n+2$ layer atoms become $(\sqrt{2}/4) a$. This corresponds to a compressive strain of 18%.

Now consider the $\langle 111 \rangle$ situation as shown in Fig. 19. Between layers n and $n+1$, $n+2$ and $n+3$, $n+4$ and $n+5$, etc., the atoms are connected by three bonds while there is only one bond between planes $n+1$ and $n+2$, $n+3$ and $n+4$, $n+5$ and $n+6$, etc. Based on this relationship we assume that the polishing removes atoms such that the single rather than triple bonds are broken, i.e., all the planes up to and including $n+1$ are removed. Thus, the atoms of layer $n+2$ will be pulled toward the $n+3$ plane. Again, if the former atoms are displaced completely onto the latter the bond distance become $(1/\sqrt{6}) a$, corresponding to a compressive strain of about 6%.

The above analysis indicates that the polishing should produced a compressive strain and that the ratio on the $\langle 100 \rangle$ to $\langle 111 \rangle$ surfaces should be a factor of three. Both these deductions are in good agreement with our experimental results. However, the absolute strain predicted by assuming complete displacement is significantly larger than our observations. For

example, For the $\langle 100 \rangle$ surface 18% (predicted) to 2-3% (observed). This indicates that there may not be complete displacement or that our model is too simple to account for these quantitative details.

b. Diffusion Model

From Fig. 16 and 17 as well as Tables II and III we note for GaAs $\langle 100 \rangle$ and $\langle 111 \rangle$ that d_s is a function of polishing time t and that for both situations it saturates with increasing time. This time dependence of d_s can be explained on the basis of a diffusion model which will yield a diffusion constant, κ , for a given polishing condition.

We assume that there are two types of processes occurring during the polish procedure. The first is the strain is created at the surface and diffuses into the material perpendicular to the surface. The second process is the removal of the surface layers during the polish operation. The surface strain provides a driving force, so that the strain is propagated into the sample. For simplicity, we assume that the diffusion occurs in only one dimension, that is:

$$(\partial \Delta \omega / \partial t) = \kappa (\partial^2 \Delta \omega / \partial x'^2) \quad (23)$$

where $\Delta \omega$ is the shift in the LO phonon frequency from its unstrained value, t is the polish time, x' is the spatial coordinate perpendicular to the surface whose origin is at the surface when $t=0$, and κ is a diffusion constant. We can express the removal of surface layers during the polishing in terms of the equation,

$$x' = x + Ct \quad (24)$$

where C is the rate of surface removal and x is the distance from surface at time t . Combining Eqs.(15) and (16), we get the differential equation:

$$(\partial \Delta \omega / \partial t) = \kappa (\partial^2 \Delta \omega / \partial x'^2) + C (\partial \Delta \omega / \partial x) \quad (25)$$

Our boundary conditions are:

$$\Delta \omega(x, 0) = 0 \quad x > 0 \quad (26a)$$

From experiment, when $t > 2.5$ minutes, the strain at the surface is almost independent of the time (see Tables II and III) so that we can write:

$$\Delta\omega(0,t) = \Delta\omega_0 \quad t > 2.5 \text{ minutes} \quad (26b)$$

In order to solve Eq.(12) we make the addition assumption that:

$$\Delta\omega(0,t) = \Delta\omega_0 \quad \text{for } t > 0 \quad (26c)$$

Also from experiment,

$$\lim_{t \rightarrow \infty} \Delta\omega(x,t) = 0 \quad (26d)$$

From the above boundary conditions the solution to Eq.(12) can be written as:

$$\Delta\omega = \Delta\omega_0 f(x;t,d_m) \quad (27a)$$

where

$$f(x;t,d_m) = \exp(-x/d_m) \{1 - (2/\pi) \exp(x/2d_m) \int_0^{x/2\sqrt{\kappa t}} d\eta \exp[-\eta^2 - x^2/(16d_m^2 \eta^2)]\} \quad (27b)$$

and

$$d_m = \kappa/C \quad (27c)$$

It is clear that the mathematical form of Eq.(27a) is different from Eq.(9a), the expression that we have used to interpret our data. We will show that the difference between the two forms is negligible for $t > 2.5$ minutes, i.e. the shortest time used in this work. That is, we will demonstrate the Eq.(27b) can be approximated by a simple exponential (for $t > 2.5$ minutes):

$$f(x;t,d_m) \approx \exp[-x/d_s^{\text{eff}}(t)] \quad (28)$$

In the limit of long polishing time it can be shown from Eq.(27b) that Eq.(20) is rigorous. That is:

$$\lim_{t \rightarrow \infty} f(x; t, d_m) = \exp(-x/d_m) \quad (29a)$$

and hence

$$d_m = d_s(\infty) \quad (29b)$$

Note that in Figs. 16 and 17 as the time increases d_s saturates, in general agreement with the above consideration. Hence, from the experimental saturation value of d_s we can evaluate d_m .

In order to plot $f(x; t, d_m)$ it is necessary to know not only d_m but also the parameter C . To evaluate this quantity we polished GaAs <100> and <111> surfaces with 0.05 μm grit for 30 minutes and measured the weight loss of the samples which had given surface areas. From this procedure we obtain:

$$\begin{aligned} C^{100} &= (6.1 \pm 0.2) \times 10^{-4} \text{ cm/sec} \\ C^{111} &= (5.1 \pm 0.2) \times 10^{-4} \text{ cm/sec} \end{aligned}$$

Using the value of C^{100} given above and estimating $d_m = 200\text{\AA}$ from Fig. 6, we have calculated $f(x; t, d_m)$ as a function of x for $t = 2.5$ minutes; these results are plotted as the solid line in Fig. 20. In order to determine the validity of Eq.(28), we have made a least square fit of the right hand side of Eq.(28) (a simple exponential form) to $f(x; 2.5\text{min}, 200\text{\AA})$. This fit is displayed as the solid line in Fig. 20. The least square fit the simple exponential is shown by the dashed line Fig. 20. There is relatively little difference between two curves. This fitting procedure yields $d_s^{\text{eff}}(2.5\text{min}) = 110\text{\AA}$. The chi-square in this fitting procedure is about 2.1, indicating that fit is quite good. From the use of the simple exponential [Eq.(1a)] in our original analysis we have obtained $d_s = 100\text{\AA}$ for this polishing condition (see Table II). Thus $d_s^{\text{eff}} \approx d_s$ and hence there is little error in using a simple exponential [Eq.(10)] instead of the more rigorous form of Eq.(19b) in evaluating the skin depth of the polish-induced damage. Obviously for $t > 2.5$ minutes there is even a closer correspondence between $f(x; t, d_m)$ and the simple exponential as indicated by Eq.(29a).

Using the value of C^{111} given above and estimating $d_m = 440\text{\AA}$ from Fig. 17, we have calculated $f(x; 2.5\text{min}, 440\text{\AA})$ as a function x for the <111> case. The result is plotted as the solid line in Fig. 21. As in the case of the <100> sample, we also have made a least square fit of the right side Eq.(28) to $f(x; 2.5\text{min}, 440\text{\AA})$. The least square fit of the simple exponential is shown by

the dashed line in Fig.21. There is also relatively little difference between two curves.

In order to show that the analysis based on the one dimensional diffusion model is consistent with the experiment for different polishing times, in Fig. 16 we have plot $d_s^{eff}(t)$ versus t from 2.5 to 60 minutes as evaluated by the above comparison procedure for the case of $d_m=200\text{\AA}$ (solid line) and $d_m=175\text{\AA}$ (dotted line) for $\langle 100 \rangle$ GaAs damaged with $0.05\mu\text{m}$ grit. The values of $d_s(t)$ were obtained by a least square fit of Eq.(10) to the set of data $\Delta\omega$ which are generated by Eq.(27b) with a particular value of d_m . We find that $d_m=175\text{\AA}$ yields a better overall fit to the experimental results. This value is well within the error bars for the experimentally determined $d_s(t)$.

In Fig. 17, we have plotted $d_s^{eff}(t)$ versus t from 2.5 to 60 minutes for the case of $d_m=440\text{\AA}$ (solid line) and $d_m=400\text{\AA}$ (dotted line) for $\langle 111 \rangle$ GaAs damaged with $0.05\mu\text{m}$ grit. The values of $d_s^{eff}(t)$ were obtained by a least square fit of Eq.(10) to the set of data $\Delta\omega$ which are generated by Eq.(27b) with a particular value of d_m . The dotted line ($d_m=400\text{\AA}$) fits the experiment better than solid line ($d_m=440\text{\AA}$). For $t < 10$ minutes, the fitting is not good as for the $\langle 100 \rangle$ case (see Fig. 16) This may be because the effect of inhomogeneous strain for $\langle 111 \rangle$ surface is negligible, affecting the experimental value of d_s . For long polish times, the effect of inhomogeneous strain is probably not a major factor and hence there is a better fit.

Using Eq.(27c) the diffusion constants for the $\langle 100 \rangle$ and $\langle 111 \rangle$ directions are evaluated to be:

$$\begin{aligned}\kappa^{100} &= (1.07 \pm 0.05) \times 10^{-9} \text{ cm}^2/\text{sec} \\ \kappa^{111} &= (2.04 \pm 0.21) \times 10^{-9} \text{ cm}^2/\text{sec}\end{aligned}$$

using $d_m=175\text{\AA}$ for the $\langle 100 \rangle$ surface and $d_m=400\text{\AA}$ for the $\langle 111 \rangle$ case, respectively. The diffusion constant for the $\langle 111 \rangle$ surface is about twice as large as $\langle 100 \rangle$, indicating that the propagation of the strain along the former direction occurs more readily in relation to the latter. In the spring model discussed above the bond-breaking for the $\langle 111 \rangle$ surface is easier than for $\langle 100 \rangle$. Therefore the bond-breaking and diffusion models are in qualitative agreement.

c. Disorder and Temperature Gradient Effect

It has been shown that the influence of disorder and/or temperature gradients on the LO phonon is to red shift the peak position and asymmetrically (low-frequency side) broaden the line shape²⁷. Introducing such an effect into our equations yields a poorer fit. We have measured the RS below the LO phonon region and find little disorder-activated effects⁵⁸. With regard to temperature, we used the same power for both damaged and undamaged surfaces and so have no reason to suspect a difference in temperature gradient in these cases. We concluded that the effects of disorder and temperature gradient are relatively minor.

d. Free Carrier Effects

There is also the question of whether or not our blue shift (of about $5\text{-}10\text{cm}^{-1}$) is due to the introduction of free carriers^{30,62,63} by the polish damage. It is well known that the L_+ component of the coupled plasmon-LO phonon mode is at a higher frequency than that of the uncoupled LO peak¹⁶. If the scattering volume near the polished sample surface contains a free carrier concentration of $n=1.0\times 10^{17}\text{cm}^{-3}$, then L_+ will lie about 10 cm^{-1} higher than uncoupled LO mode (292 cm^{-1}). Thus it might be responsible for the high frequency bump in the damaged spectra of Fig.11(a) and 11(b). This ambiguity can be resolved by examining the TO phonon since this mode does not couple to the free carriers. We measured the TO phonon RS from the $\langle 111 \rangle$ damaged surfaces and observed a blue shift from its unstrained value. However, because of the complexities of the strain-dependence of the TO phonon (it is a doublet)^{40,60}, we were not able to do a detailed fit. The observed blue shift is consistent with the strain-induced shift of the LO mode and hence we deduce that free -carriers are not a factor in our analysis.

e. Dislocations and Point Defects

In addition to the strain due to the bond-breaking discussed above, strain due to the dislocations and point defects such as vacancies and interstitials, may exist⁶⁴. It is known that the dislocations and point defects are created by polish damage and that vacancies and interstitials exist as intrinsic defects. Vacancies are strong centers of attraction, producing tensile stress in the lattice, while interstitials create

repulsion, producing compressive stress in the lattice. The creation of a vacancy and interstitial is simultaneous, e.g., there are equal amounts of vacancies and interstitials. Therefore, the macroscopic strain due to vacancies and interstitials should cancel each other. Hence the strain due to the point defects is not measurable in this study. The strain due to the dislocations is a shear stress. The dislocations may make a contribution to the strain in the sample. However, since we have not evaluated the dislocation density (by a technique such as TEM) for the various polishing conditions we cannot comment on any possible relationship between our observed strains and the dislocations. This point certainly warrants further investigation.

f. Comparison with Previous Investigations

For the $\langle 111 \rangle$ case our results are consistent with those of other investigators^{57,58}, including Evens and Ushioda. As shown in Table II we find that the strain skin depth for both materials is approximately equal to the polishing particle size (for GaAs δ_s is somewhat smaller than the particle size). Also, for both semiconductors δ_s become larger with increasing polishing time. The phonon line broadening is caused primarily by the inhomogeneous strain distribution (both compressive and tensile) in the polishing plane, while the shift of the RS peak is due to the mean compressive surface strain.

For the $\langle 100 \rangle$ case our findings are somewhat different from those of other investigators^{50,51,53,57,65}. Other workers have concluded that the strain penetration depth is on the order of the particle size. However, they did not examine the $\langle 100 \rangle$ orientation but reported on other faces. Also, some of the earlier studies were not "non-destructive" but obtained their findings by etching away controlled amounts of material from the surface. We find that strain penetration depth for the $\langle 100 \rangle$ surface is considerably less than the particle size, particularly in the 0.3 μm and 1 μm cases (see Table I). Compared with the $\langle 111 \rangle$ surface case, the strain in the $\langle 100 \rangle$ surface is relatively homogeneous. The phonon line broadening is primarily due to the exponential decay of homogeneous strain from surface.

For $\langle 100 \rangle$ GaAs our study agrees with the $\langle 100 \rangle$ GaAs study of Kuwamoto et. al.⁵⁷. They have used X-ray diffraction, RS and TEM to investigate work damage created during standard processes used to fabricate GaAs wafers.

Equation (a) was used to evaluate the skin depth while the concentration of dislocations was estimated by cross-sectional TEM analysis. The skin depth of damage evaluated by X-ray, Raman and TEM were found to be in quantitative agreement.

E. Excitation Wavelength and Pump Chopping Frequency Dependence of Photoreflectance in $\text{Hg}_{1-x}\text{Cd}_x\text{Te}$

We have measured photoreflectance (PR) at 77K in the vicinity of the E_1 optical feature from $\text{Hg}_{1-x}\text{Cd}_x\text{Te}$ ($0.14 < x < 0.3$) using infrared ($3.39 \mu\text{m}$) and deep blue-violet (4579Å and 4067Å) pump beams; both n- and p-type materials were investigated⁶⁶. The spectral lineshapes were fit using existing theories of electromodulation yielding interband energies and broadening parameters. In addition, the dependence of the PR intensity on the modulation frequency (Ω_m) was studied in order to obtain information regarding surface (interface) traps. The variation of PR intensity with Ω_m yielded characteristic trap time constants in the range 1-4 milliseconds.

In PR the electric field that may occur at the surface (interface) of a semiconductor (or semiconductor structure) is modulated by the photo-injection of electron-hole pairs by a secondary (pump) beam chopped at frequency Ω . The measured PR spectra are very similar to corresponding ER features.^{67-70,71,72} It has been demonstrated that the mechanism of PR is indeed electromodulation.^{73,74} Thus PR features can be analyzed using existing theories of electromodulation^{69,73-75}. Information about the material and/or structure can be obtained from the details of the lineshape (energy positions, broadening parameters, etc.) as well as the response to the modulation (pump) perturbation (pump wavelength, modulation frequency,⁷⁶⁻⁷⁸ modulation amplitude,^{71,72} etc.). While considerable attention has been devoted to lineshape features little work has been done in the latter area.^{76,78} Recently, the recombination lifetime of electron-hole pairs in GaAs compositional superlattices was obtained from the variation of the PR intensity with Ω_m ⁷⁷. Amirtharaj et al have recently reported the first PR study of $\text{Hg}_{1-x}\text{Cd}_x\text{Te}$ and $\text{Cd}_{1-x}\text{Zn}_x\text{Te}$.⁷⁶ For the former material the $3.39 \mu\text{m}$ line of a He-Ne laser was employed as the pump excitation with a power density of about 5 mW/cm^2 .

In this study we report the results of a PR study at 77K of $\text{Hg}_{1-x}\text{Cd}_x\text{Te}$ ($0.14 < x < 0.3$) using as pump excitation sources the 4067Å line of a Kr^+

laser 4579A line of an Ar^+ laser, or the 3.39 μm line of a He-Ne laser.⁶⁵ No PR signal could be obtained for pump wavelengths in the visible with an energy below the E_1 optical transition. The spectra were studied in the region of the E_1 optical structure. The lineshapes were analyzed using currently available theories of Aspnes⁷ and Raccah yielding interband energies and broadening parameters.^{73,75} In addition, for several samples we have investigated the dependence of the PR intensity on pump chopping frequency, Ω_m . An analysis of this variation yields a characteristic time which can be related to slow surface (interface) traps.⁷⁶

1. Experimental Details

The experimental apparatus used to measure the PR signal, $\Delta R/R$, was similar to that described in Refs. 71 and 72. In addition to recording the output on a chart recorder the signals were also digitized and stored on a computer for analysis. For the measurements in the infrared the 3.39 μm line of a He-Ne laser was employed while the deep blue-violet experiments were carried out using lines of an Ar^+ or Kr^+ laser in the range 4579-4067A. Typical power densities were 5 mW/cm^2 for the infrared and 100 mW/cm^2 for the deep blue-violet. All measurements were made at 77K in the vicinity of the E_1 critical point of $\text{Hg}_{1-x}\text{Cd}_x\text{Te}$ (~ 2.3 -2.5 eV). The deep blue-violet experiments in this spectral region presented some experimental problems. Because of the proximity of the pump and probe wavelengths it was not possible to completely eliminate some of the strong pump radiation from reaching the detector. Thus, the deep blue-violet spectra contained a spurious background in addition to any real background that may be present in electromodulation from $\text{Hg}_{1-x}\text{Cd}_x\text{Te}$.^{73,74,76}

Four different samples were studied including bulk, liquid phase epitaxy (LPE) and molecular beam epitaxy (MBE) material. The bulk samples were both n-type ($n \sim 10^{15} \text{ cm}^{-3}$, $x=0.3$) and p-type ($p \sim 5 \times 10^{16} \text{ cm}^{-3}$, $x=0.3$). The n-type material was achieved by annealing for about 30 days Hg overpressure. The LPE material consisted of an n-type film ($n \sim 10^{15} \text{ cm}^{-3}$) of thickness 10 μm having $x=0.22$ grown on a CdTe (111) substrate. The MBE sample, of thickness 3 μm on a CdTe (111) substrate, also was n-type ($n \sim 2.5 \times 10^{16} \text{ cm}^{-3}$) but had a nominal Cd concentration of $x \approx 0.14$. The surface of the p-type material was polished by a procedure given in Ref. 82. The surfaces of the n-type samples were not processed.

2. Experimental Results

a. LPE $\text{Hg}_{0.78}\text{Cd}_{0.22}\text{Te}$ (n-type)

The PR spectrum measured from the LPE $\text{Hg}_{0.78}\text{Cd}_{0.22}\text{Te}$ sample at 77K with the 3.39 μm pump at $\Omega_m \approx 100$ Hz is displayed by the solid line in Fig. 22. The maximum noise present in the spectrum was $\pm 10^{-8}$. The signal exhibits a typical electromodulation lineshape. Figure 23 displays the variation in the normalized PR intensity, i.e. $[\Delta R(\Omega_m)/R]/[\Delta R(0)/R]$, as a function of chopping frequency Ω_m in the range 50-1000 Hz.

The PR results using the 4067A pump on this sample are shown in Fig. 24 by the dotted curves for $\Omega_m = 103\text{Hz}$, 600Hz and 4035Hz. The spurious background due to the pump leakage has already been subtracted. The lineshapes in Fig. 24 are quite similar to that in Fig. 22. However, the amplitude of the signal is more than an order of magnitude larger. The chopping frequency dependence of the PR intensity for this case is shown in Fig. 25 in the range 40-4000 Hz.

b. MBE- $\text{Hg}_{0.86}\text{Cd}_{0.14}\text{Te}$ (n-type)

In Fig. 26 is displayed the experimental PR spectrum (dotted curve) at 77K in the region of the E_1 optical transition using 4067A pump wavelength at $f=100\text{Hz}$. The amplitude of the curve is comparable to that in Fig. 24. Note that the energy of the E_1 optical feature for this sample is lower than that of LPE - $\text{Hg}_{0.78}\text{Cd}_{0.22}\text{Te}$ due to the smaller Cd concentration.

c. Bulk $\text{Hg}_{0.7}\text{Cd}_{0.3}\text{Te}$ (n-type)

The experimental data at 77K for this sample in the region of the E_1 transition is plotted in Fig. 27 (dotted curve) using the 4067A pump for $f=100\text{Hz}$. The amplitude of the signal from this sample is somewhat smaller than those in Figs. 24 and 26.

d. Bulk $\text{Hg}_{0.7}\text{Cd}_{0.3}\text{Te}$ (p-type)

For this sample the PR spectra at 77K for $\Omega_m = 84\text{Hz}$, 641Hz and 3215Hz using the 4067A pump are shown in Fig. 28 by the dotted curves. The PR signal at 77K using the 4579A line of an Ar^+ laser is displayed in Fig. 29. We were not able to get a PR signal from this sample (or any of the other materials) for pump wavelengths in the green-blue, i.e. Ar^+ laser lines in

the range 5145Å-4880Å, even with power densities ($\sim 100 \text{ mW/cm}^2$) comparable to the 4067Å or 4579Å lines. Thus, for pump photon energies below E_1 no PR was observed. In Fig. 30 we have plotted $[\Delta R(\Omega_m)/\Delta R]/[\Delta R(0)/R]$ as a function of Ω_m for this sample. Note that the frequency variation for this sample is less than that for the LPE material (see Fig. 25).

3. Analysis and Discussion

a. Lineshape Analysis

It has recently been shown that electric-field modulated reflectivity line shape, $\Delta R/R$, in the low-field regime for $\text{Hg}_{1-x}\text{Cd}_x\text{Te}$ can be fit by a generalized derivative functional form (GDFF) given by:^{73,75}

$$\Delta R/R = \sum C_j E^{-2} [(\hbar\Omega_j)^3 L^{(3)}(n,E) - 4\Delta\sigma_j L^{(2)}(n,E) - 4\Delta E_j L^{(1)}(n,E)] \quad (30)$$

where E is the photon energy, p is the number of spectral features to be fit and C_j is the amplitude of the j^{th} feature. The quantity $L^{(M)}(n,E)$ is the lineshape function, with n depending on the dimensionality of the critical point. The lineshape function can be expressed as:

$$L^{(M)}(n,E) = \frac{\cos [\theta - (M-n)\varphi]}{[(E-E_1)^2 + \Gamma_1^2]^{(M-n)/2}} \quad (31)$$

In Eq. (31) θ is a phase factor, Γ_1 is the phenomenological broadening parameter associated with the E_1 optical transition and φ is given by:

$$\varphi = \tan^{-1} [\Gamma_1/(E-E_1)] \quad (32)$$

The other parameters in Eq. (30) are defined in Refs. 73 and 74.

The first term in Eq. (30) is the third-derivative functional form (TDFF) derived by Aspnes with C_j and $\hbar\Omega_j$ being related to the details of the critical point and applied electric field. The second and third terms have been introduced to account for the background observed in the electromodulation spectra from highly defective $\text{Hg}_{1-x}\text{Cd}_x\text{Te}$ and from the A and B faces of $\langle 111 \rangle$ CdTe.

The dashed curve in Fig. 22 is a least-squares fit of Eq. (30) to the experimental data (solid line). The obtained values of E_1 and Γ_1 are listed in Table IV. For this sample we have found $\Delta\sigma^2/(\hbar\Omega)^3 = 1.28 \text{ eV}^{-1}$ and $\Delta E_1/(\hbar\Omega)^3 = 0.054 \text{ eV}^{-2}$. These quantities are relatively small, indicating

the material is fairly free from defects. However, the broadening parameter Γ_1 is somewhat larger than the best values (~ 70 meV) reported for $\text{Hg}_{1-x}\text{Cd}_x\text{Te}$ at 77K of comparable composition.^{76,79}

For the measurements made with the 4067A pump wavelength there is a spurious background due to stray pump radiation reaching the detector. This background makes it difficult to distinguish between GDF and TDF fits to the experimental curves. For all data taken under this condition we have found that both lineshape forms yield comparable results.

The solid lines in Figs. 22, 24, 26 and 28 are a least-squares fit of Eq. (30) to the experimental data. The obtained values of E_1 and Γ_1 also are listed in Table IV. We do not report the coefficients for $L^{(2)}(n,E)$ and $L^{(1)}(n,E)$ since their interpretation is not clear due to the spurious background mentioned above.

For the LPE- $\text{Hg}_{0.78}\text{Cd}_{0.22}\text{Te}$ material the values of both E_1 and Γ_1 are about 10% different for the 3.39 μm and 4067A pump wavelength measurements. This may be due to sample inhomogeneity since no care was exercised to insure that both measurements were taken on the same spot on the sample. The energy of E_1 is consistent with a $x \approx 0.22$.

The MBE- $\text{Hg}_{0.86}\text{Cd}_{0.14}\text{Te}$ sample has E_1 consistent with $x \approx 0.14$ and a broadening parameter comparable to the LPE sample.

Both bulk- $\text{Hg}_{0.7}\text{Cd}_{0.3}\text{Te}$ samples (n-type and p-type) had essentially the same value of E_1 . The PR results of Amirtharaj et al at 77K on LPE- $\text{Hg}_{0.7}\text{Cd}_{0.3}\text{Te}$ has yielded a similar value for E_1 .⁷⁶ The quality of the n-type sample does not appear to be very good since it has $\Gamma_1 = 146$ meV. Of all the samples studied the bulk p-type sample appears to be the best with $\Gamma_1 = 79$ meV. However, even this value is not as good as previously reported 77K^{76,79} (or even 300K⁷³) measurements.

b. Pump Frequency Dependence of the PR Intensity

The dependence of the PR intensity as a function of the chopping frequency was studied with a view towards obtaining information about the dynamics of the surface electric fields. This variation can be accounted for on the basis of the following considerations. The chopped pump radiation can be considered as a square wave source. When light impinges on the sample, electron-hole pairs are created. These charges are then free to fill the charge traps and modify the surface electric field strength.

somewhat similar to the behavior of a capacitor. We assume that these excess carriers abruptly change the build-in electric field. When the light is switched off the trap population and the electric field strength decays with a characteristic time τ , causing a restoration of the original surface potential. Thus for chopping frequency f it can be shown that the Fourier component of the PR intensity, $\Delta R(\Omega_m)/R$, can be written as:^{77,81}

$$\Delta R(\Omega_m)/R = \Delta R(0)/R \sum_{i=1}^n \frac{4 + \Omega_m^2 \tau_i^2 [1 - \exp(-\pi/\Omega_m \tau_i)]^2}{4(1 + \Omega_m^2 \tau_i^2)} \quad (33)$$

where τ_i is the characteristic time constant of the i^{th} trap state.

As an appropriate means to extract the effective average time constant τ from the observed modulation frequency dependence of the PR intensity we have used a modified version of Eq. (32):

$$\frac{\Delta R(\Omega_m)/R}{\Delta R(0)/R} = \frac{4 + \Omega_m^2 \tau^2 [1 - \exp(-\pi/\Omega_m \tau)]^2}{4(1 + \Omega_m^2 \tau^2)} + A \quad (34)$$

The term A in Eq. (33) represents the contribution from all the states with $1/\tau \gg 1000\text{Hz}$, i.e., very fast states in relation to our frequency range.

The solid lines in Figs. 23, 25 and 29 represent a least-squares fit of Eq. (34) to the experimental data points. The obtained values of τ are listed in Table V. All three measurements yield time constants on the order of milliseconds. This is consistent with the large number ($\sim 10^{13} \text{ cm}^{-2}$) of slow traps with $\tau \geq 1$ millisecond observed at the HgCdTe/oxide interface using capacitance-voltage techniques.⁸² It should be noted, however, that the LPE $\text{Hg}_{0.78}\text{Cd}_{0.22}\text{Te}$ data presented in Fig. 23 obtained using the $3.39 \mu\text{m}$ pump radiation contains a large constant background which indicates the presence of a significant number of "fast" traps in addition to the $\tau = 4.4$ msec slow traps. The frequency response of the PR intensity from the same sample recorded using the 4067\AA pump wavelength indicated a dominant trap level with $\tau = 2.8$ msec (see Fig. 23). The apparent differences observed with these two pump wavelengths may be an indication of the variation in the details of the charging and discharging of the traps within the region penetrated by the two pump beams. For instance, traps within about 100\AA of the surface and in the native oxide layer will play a more important role in the case of the 4067\AA pump due to its short penetration depth ($\sim 200\text{\AA}$).

F. $\text{Hg}_{0.7}\text{Cd}_{0.3}\text{Te}/\text{SiO}_2$ -Photox Interface Properties Studied by Photo- and Bias-Induced Charging

We have investigated the effects of light illumination in the wavelength range $1\mu\text{m}$ - 2200\AA (with and without dc bias) on the $\text{Hg}_{0.7}\text{Cd}_{0.3}\text{Te}$ (n-type)/ SiO_2 -PhotoxTM interface at 77K in the metal-insulator-semiconductor device configuration⁸³. Illumination of wavelength λ without bias produced a flatband shift (ΔU_{fb}) towards positive values. The saturation value of ΔU_{fb} has a pronounced peak at $\lambda \approx 2800\text{\AA}$ and is negligible for $\lambda \geq 5100\text{\AA}$. The light-induced charge is maintained for at least 8 hours at 77K but leaks off if the device is heated briefly to 300K. We propose a model to explain these results involving light-induced charging and discharging of very slow trap states in the SiO_2 -PhotoxTM (at or near the interface) with an energy distribution centered about 4.5 eV above the oxide valence band. With a positive gate voltage charging is extended to wavelengths of $1\mu\text{m}$ (limit of our measurements), the resulting charge quickly leaking off. This latter effect is related to charging of faster interface states that are apparently different from the slow states discussed above.

Passivation of $\text{Hg}_{1-x}\text{Cd}_x\text{Te}$ by deposition of a foreign insulator such as SiO_2 -PhotoxTM has become technologically important due principally to its chemical inertness coupled with the resultant high quality interfaces [86]. It is important to have information about interface traps since they can limit the carrier lifetimes in junction devices or, when charged, alter the effective gate bias of metal-semiconductor-insulator (MIS) devices. The $\text{Hg}_{1-x}\text{Cd}_x\text{Te}$ interface in the MIS configuration has been studied in the frequency range 1 - 10^7 Hz [87-90]. Work in the 1 - 10^3 Hz region on the $\text{Hg}_{1-x}\text{Cd}_x\text{Te}/\text{SiO}_2$ -PhotoxTM interface [90] revealed a considerable number of interface traps ($\geq 10^{13} \text{ cm}^{-2}\text{-eV}^{-1}$). Illumination effects in the very low frequency domain ($\sim 10^{-5}$ Hz) on $\text{Hg}_{1-x}\text{Cd}_x\text{Te}$ MIS devices fabricated with a native oxide⁸⁸ indicated a total trap density in the oxide as high as $6 \times 10^{13} \text{ cm}^{-2}$. We have recently reported electroreflectance results at 77K on a $\text{Hg}_{0.7}\text{Cd}_{0.3}\text{Te}/\text{SiO}_2$ -PhotoxTM MIS structure⁸¹

1. Experimental Details

The structure used in this experiment consisted of the same MIS device used in Ref. 81. All light-induced studies were carried out at 77K. To provide illumination we used light from a xenon lamp passed through a 0.3

meter grating monochromator (GCA/McPherson model 218). In order to find the photon flux (at λ) the power of the monochromatic light was first measured at 5100Å with a light power meter (International Light Power meter model 1L510) and then the calibration was extended to shorter wavelengths using a Si photodiode (EG&G model 4000B) with a known spectral response curve. The charging of the $\text{Hg}_{0.3}\text{Cd}_{0.7}\text{Te}/\text{SiO}_2$ -PhotoxTM interface was determined by C-V measurements at a frequency of 1 kHz, the amplitude of the ac probe voltage at the gate being 50 mV.

2. Experimental Results

a. Light Illumination at Zero Bias Voltage

The sample (in the open circuit configuration) was first illuminated by light at λ from the monochromator for a given amount of time (t). The C-V measurements were then taken in the dark. After this procedure a new illumination period was started.

From the C-V measurement we have established that if the sample was kept at 77K in the dark after the above illumination procedure, the light-induced charge remained unchanged for at least 8 hours. This demonstrates that the trap mechanism is very slow with a characteristic frequency $< 10^{-5} \text{ sec}^{-1}$. Thus after every new illumination period we have actually measured the cumulative effect of all preceding illumination periods. After U_{fb} reached a value of 20 V (or at the end of the day, whichever came first) the sample was heated to 300K which restored it to the initial, uncharged state. This was checked by cooling the sample down to 77K and taking C-V measurements after the 30 minute heating procedure.

In Fig. 31 we present a typical set of C-V curves from our sample after illumination by 2800Å light for different periods of time. The value of U_{fb} in each measurement was determined to be the voltage corresponding to a capacitance of 375 pF^{89}

Plotted in Fig. 32 is the light-induced flatband shift, ΔU_{fb} , as a function of the total number of incident photons per unit area, $P(\hbar\omega)$, for three different wavelengths. The inset shows an expanded version of the 2800Å data. Note that for all three wavelengths ΔU_{fb} tends to saturate as P increases. The saturation level for ΔU_{fb} peaks at $\lambda = 2800\text{Å}$ while for $\lambda \geq 5100\text{Å}$ we have found no significant light-induced charging.

b. Light Illumination with Gate Bias

Application of a negative bias to the gate produced no appreciable change in the charging picture described above. However, the application of a positive bias made it possible to charge the system by utilizing $\lambda > 5100\text{\AA}$. The result of illuminating the structure by $\lambda = 1\mu\text{m}$ light is presented in Fig. 33. Curve (1) is the C-V measurement with no light exposure and no bias; this curve is the same as the $t=0$ data of Fig. 31. The C-V results after exposure to $1\mu\text{m}$ light for one hour and a gate bias of $+10\text{ V}$ is shown in curve (2). The light and the dc bias were then shut off and the C-V evaluated after 10 minutes in the dark as displayed in curve (3). The results of Fig. 33 indicate that 1 hour of illumination under $+10\text{ V}$ bias has increased U_{fb} from approximately 1 V to 4 V . Figure 33 shows that the charge leaks off relatively quickly since after only 10 minutes of relaxation at 77 K in the dark U_{fb} was reduced to about 2 V from 4 V . This is in sharp contrast with the case of charging by illumination only and suggests a different charging mechanism when bias is applied.

3. Discussion

a. Charging by Light Illumination with Zero Bias Voltage

The results of Figs. 31 and 32 can be explained by the presence of very slow electron traps at or near the $\text{Hg}_{0.7}\text{Cd}_{0.3}\text{Te}/\text{SiO}_2\text{-Photox}^{\text{TM}}$ interface. The fact that the photo-induced flatband shift has a maximum for $\lambda \approx 2800\text{\AA}$ suggests that two mechanisms are operative; i.e., both charging and discharging. For $2800\text{\AA} \leq \lambda \leq 5100\text{\AA}$ the light creates only a charging effect while for $\lambda \leq 2800\text{\AA}$ both charging and discharging occur. In addition, there is a distribution of trap states so that as the photon energy increases (up to a certain point) the number of traps accessed by the charging mechanism also increases, which explains why the 2800\AA light creates a greater ΔU_{fb} than say 3300\AA . With further increase of the photon energy the discharging mechanism also comes into play and causes the 2200\AA light to be less effective.

The above mechanisms are illustrated in further detail in Fig. 34. In this figure we display schematically the interfacial region of the $\text{Hg}_{0.7}\text{Cd}_{0.3}\text{Te}/\text{SiO}_2\text{-Photox}^{\text{TM}}$ system. The energy gaps of the two materials are denoted as $E_{g,1}$ ($\text{Hg}_{0.7}\text{Cd}_{0.3}\text{Te}$) and $E_{g,2}$ (SiO_2). The zero of energy is taken to be the top of the SiO_2 valence band. The electron traps are distributed

continuously with distribution $D_t(E)$ around energy E_0 with full-width at half-maximum of δE_0 . The n-type $\text{Hg}_{0.7}\text{Cd}_{0.3}\text{Te}$ is slightly depleted as indicated by the positive value of U_{fb} in the dark ($t=0$ curve in Fig. 1). For the sake of clarity the band gaps of the $\text{Hg}_{0.7}\text{Cd}_{0.3}\text{Te}$ (~250 meV) and the SiO_2 (9 eV) are not drawn to scale.

As shown in the figure two processes can occur:

- (1) Charging - An electron can be photo-excited from the SiO_2 valence band into a trap state, some of the resultant holes moving into the $\text{Hg}_{0.3}\text{Cd}_{0.7}\text{Te}$ region. This process can take place for photon energies ($\hbar\omega$) less than or equal to $E_{g,2}$. We denote the quantum efficiency of this process as Q_1 .
- (2) Discharging - For photon energies greater than $E_{g,2}/2$ not only does charging take place as discussed above but, in addition, electrons in the trap states can be photo-excited into the conduction band of the SiO_2 . Some of these electrons can be transferred into the conduction band of the $\text{Hg}_{0.7}\text{Cd}_{0.3}\text{Te}$. The quantum efficiency of this effect is denoted as Q_2 .

Note, that in order for process (1) to cause charging, the photoexcited hole must move into the $\text{Hg}_{0.3}\text{Cd}_{0.7}\text{Te}$ against the action of electric field whereas in process (2) the excited electron which produces discharging is pulled towards the $\text{Hg}_{0.3}\text{Cd}_{0.7}\text{Te}$ by the electric field. Thus we expect process (2) to have a higher probability than process (1), i.e. $Q_2 \gg Q_1$.

We denote as N_1 the number of states per unit area available to mechanism (1) but not mechanism (2) and as $N_{1,2}$ the number of states available to both (1) and (2). We can write:

$$N_1(\hbar\omega) = \begin{cases} \hbar\omega \\ \int_0^{\hbar\omega} D_t(E) dE \end{cases} \quad \hbar\omega < E_{g,2}/2 \quad (35a)$$

$$N_1(\hbar\omega) = \begin{cases} E_{g,2} - \hbar\omega \\ \int_0^{E_{g,2} - \hbar\omega} D_t(E) dE \end{cases} \quad \hbar\omega > E_{g,2}/2 \quad (35b)$$

$$N_{1,2}(\hbar\omega) = \begin{cases} 0 \\ \hbar\omega \end{cases} \quad \hbar\omega < E_{g,2}/2 \quad (36a)$$

$$N_{1,2}(\hbar\omega) = \begin{cases} \hbar\omega \\ \int_0^{\hbar\omega} D_t(E) dE \\ E_{g,2} - \hbar\omega \end{cases} \quad \hbar\omega > E_{g,2}/2 \quad (36b)$$

In Fig. 34 the dark region corresponds to N_1 while the shaded region represents $N_{1,2}$. In order to develop our model more fully we define the following quantities:

$n_1(n_{1,2})$ = number of traps per unit area filled in the $N_1(N_{1,2})$ part of the trap distribution.

n = total number of filled traps per unit area.

Therefore, for process (1) we can write:

$$dn_1/dt = Q_1(P/t) (N_1 - n_1) \quad (37)$$

while for process (1) and (2):

$$dn_{1,2}/dt = Q_1(P/t) (N_{1,2} - n_{1,2}) - Q_2(P/t)n_{1,2} \quad (38)$$

The solutions to Eqs. (3) and (4) can be written as:

$$n_1(P) = N_1[1 - \exp(-Q_1P)] \quad (39)$$

$$n_{1,2}(P) = [N_{1,2}Q_1/(Q_1+Q_2)] \{1 - \exp[-(Q_1+Q_2)P]\} \quad (40)$$

and

$$n[P(\hbar\omega)] = n_1[P(\hbar\omega)] + n_{1,2}[P(\hbar\omega)] \quad (41)$$

Equations (39), (40) and (41) show that $n[P(\hbar\omega)]$ saturates as $P \rightarrow \infty$. We denote the saturation value of $n[P(\hbar\omega)]$ as $n_s(\hbar\omega)$, such that from Eqs. (39), (40) and (41):

$$n_s(\hbar\omega) = N_1(\hbar\omega) + [N_{1,2}(\hbar\omega)Q_1/(Q_1 + Q_2)] \quad (42)$$

It is also convenient to express $n[P(\hbar\omega)]$ in terms of $n_s(\hbar\omega)$ as follows:

$$n[P(\hbar\omega)] = n_s[1 - \exp(-Q_1P)] + [N_{1,2}Q_1/(Q_1+Q_2)] \{\exp(-Q_1P) - \exp[-(Q_1+Q_2)P]\} \quad (43)$$

Comparison can thus be made between the experimental results of Fig. 32 and our model. Assuming for simplicity that the charging takes place near the insulator/semiconductor interface, the photo-induced flatband shift, ΔU_{fb} , can be related to the number of photo-filled traps $n[P(\hbar\omega)]$ by the relation

$$\Delta U_{fb}[P(\hbar\omega)] = |e|n[P(\hbar\omega)]/C \quad (44)$$

where C is the capacitance of the insulator (SiO_2) layer. Thus ΔU_{fb} can be used as a direct measure of the number of filled traps, n . From Eqs. (39)-(41) and (44) the dependence of ΔU_{fb} on $P(\hbar\omega)$ can be fit using as adjustable parameters N_1 , $N_{1,2}$, Q_1 and Q_2 . Shown by the solid lines in Fig. 32 is a least-squares fit of the experimental data to these equations for the three different wavelengths.

The quantities N_1 , $N_{1,2}$, Q_1 , and Q_2 obtained by the above fitting procedure have a fairly large standard deviation. However, the parameter

$n_s(\hbar\omega)$ can be obtained with a high degree of reliability using Eqs. (43) and (44). Shown in Fig. 35 by the open circles is $n_s(\hbar\omega)$ determined from experiment as a function of $\hbar\omega$. Note that there is a pronounced peak at about 4.7 eV and that $n_s(\hbar\omega) \approx 0$ for $\hbar\omega < 2.4$ eV..

The photon energy dependence of $n_s(\hbar\omega)$ can be accounted for on the basis of the model in Fig. 34 and Eq. (42). From the above considerations (least-squares fit in Fig. 2) we find that $Q_2 \approx 10 Q_1$ and hence for our case Eq. (42) becomes

$$n_s(\hbar\omega) \approx N_1(\hbar\omega) + (1/10) N_{1,2}(\hbar\omega) \quad (45)$$

To calculate N_1 and $N_{1,2}$ [see Eqs. (35) and (36)], we have assumed a Gaussian distribution for $D_t(E)$ having $E_0 = 4.5$ eV and $\delta E_0 = 0.5$ eV. For $E_{g,2}$ we take 9 eV which is close to the band gap of SiO_2 . Our value of E_0 corresponds to the energy of traps in thermal SiO_2 produced by P and In impurities⁹⁰. Shown by the closed circles in Fig. 35 are the values of $n_s(\hbar\omega)$ calculated using the above procedure. There is good agreement between experiment (open circles) and theory (closed circles).

b. Charging by light illumination with positive bias voltage

As we mentioned before, application of positive gate bias extends photocharging effect towards lower energies of incident light (≈ 1.2 eV was the lowest energy of our measurements). The accumulated charge leaks off in a matter of minutes - rather quickly in comparison with the preceding case. The lower light energy limit of the effect suggests that the carrier generation by light in $\text{Hg}_{0.3}\text{Cd}_{0.7}\text{Te}$ substrate is involved. Also, the faster charge leak-off points to a different nature for interface states that hold the charge. At the present time we are not able to propose a detailed model explaining this effect.

REFERENCES

1. A. Ksendzov, P. Parayanthal, F.H. Pollak, D. Welch, G.W. Wicks and L.F. Eastman, Phys. Rev. B36, 7646 (1987).
2. J.B. Boyce and J.C. Mikkelsen, Jr., Phys. Rev. B31, 6903 (1985).
3. M.W. Muller, Phys. Rev. B30, 6196 (1984).
4. See, for example, J.L. Martins and A. Zunger, Proceedings of the Seventh International Conference on Ternary and Multinary Compounds, Snowmass, 1986.
5. A. Zunger, Appl. Phys. Letts. B29, 2051 (1984).
6. T.S. Kuan, T.F. Kuech, W.I. Wang and E.L. Wilkie, Phys. Rev. Lett. 54, 201 (1985).
7. H. Nakayama and H. Fujita, in GaAs and Related Compounds 1985, edited by M. Fujimoto, Inst. Phys. Conf. Ser 79 (Adam Hilliger, Bristol, 1986), p. 289.
8. H.R. Jen, M.J. Cherny and G.B. Stringfellow, Appl. Phys. Lett. 48, 1603 (1986).
9. A. Ourmazd and J.C. Bean, Phys. Rev. Lett. 55, 765 (1985); J.L. Martins and A. Zunger, Phys. Rev. Lett. 56, 1400 (1986).
10. G.P. Srivastava, J.L. Martins and A. Zunger, Phys. Rev. B31, 2561 (1985).
11. A.A. Mbaye, L.G. Ferreira and A. Zunger, Phys. Rev. Lett. (in press).
12. M. Ichimura and A. Sasaki, J. Appl. Phys. 60, 3850 (1986).
13. See for example, D.F. Welch, G.W. Wicks, L.F. Eastman, P. Parayanthal and F.H. Pollak, Appl. Phys. Letts. 46, 169 (1985) and references therein; A. Ksendzov, P. Parayanthal, F.H. Pollak, D. Welch, G.W. Wicks and L.F. Eastman, to be published in the Proceedings of the Seventh International Conference on Ternary and Multinary Compounds, Snowmass, 1986.
14. K. Mohammed, F. Capasso, J. Allam, A.Y. Cho and A.L. Hutchinson, Appl. Phys. Lett. 47, 597 (1985).
15. J. Singh and K.. Bajaj, Appl. Phys. Lett. 44, 1075 (1984).
16. E.F. Schubert, E.O. Gobel, Y. Hirikoshi, K. Ploog and H.J. Quersser, Phys. Rev. B30, 813 (1984).
17. J. Singh and K.K. Bajaj, Appl. Phys. Letts. 48, 1077 (1986).

18. See, for example, K.K. Bajaj and D.C. Reynolds, Proceedings of the Society of Photo-optic Instrumentation Engineers 794, 2 (1987).
19. P. Parayanthal and F.H. Pollak, Phys. Rev. Lett. 52, 1822 (1984).
20. See, for example, G. Neu, C. Verie and R. Carles, Proceedings of the Seventh International Conference on Ternary and Multinary Compounds, Snowmass, 1986, and references therein.
21. D.Kirilov and J.L. Merz, Proceedings of the Society of Photo-Optical Instrumentation Engineers (SPIE), Bellingham, 1983) 452, 9 (1983).
22. D.J. Olego, P.M. Raccah and J.P. Faurie, Phys. Rev. B33, 3819 (1986).
23. J. Menedez and M. Cardona, Phys. Rev. B29, 2051 (1984).
24. H. Ohno, C.E.C. Wood, L. Rathburn, D.V. Morgan, G.W. Wicks and L.F. Eastman, J. Appl. Phys. 52, 4033 (1981).
25. R. Sacks and H. Shen, Appl. Phys. Letts. 47, 374 (1985).
26. J. Gonzalez - Hernandez, G.H. Azarbayejana, R. Tsu and F.H. Pollak, Appl. Phys. Letts. 47, 1350 (1985).
27. K.K. Tiong, P.M. Amirtharaj, F.H. Pollak and D.E. Aspnes, Appl. Phys. Lett. 44, 122 (1984).
28. H. Richter, Z.P. Wang and L. Ley, Solid State Commun. 39, 625 (1981) and references therein.
29. R.J. Nemanich, S.A. Solin and R.M. Martin, Phys. Rev. B23, 6348 (1981).
30. W. Hayes and R. Loudon, Scattering of Light by Crystals (Wiley, New York, 1978).
31. R. Tsu, S.S. Chao, M. Izu, S.R. Ovshinsky, G.J. Jan and F. H. Pollak, J. Physi. Colloq. C4 42, 269 (1981).
32. C. Kittel, Introduction to Solid State Physics, 5th Ed. (Wiley, New York, 1976), p.171.
33. H. Shen and F.H. Pollak, Appl. Phys. Lett. 45, 692 (1984).
34. R. Tsu, J. Gonzalez - Hernandez, S.S. Chao and D. Martin (unpublished).
35. H. Shen, P. Parayanthal, F.H. Pollak, R.N. Sacks and G. Hickman, Solid State Comm. 63, 357 (1987).
36. H. Shen, F.H. Pollak and R.N. Sacks, Proceedings of the Society of Photo-optical Instrumentation Engineers (SPIE, Bellingham, 1985) 524, 145 (1985).
37. H. Shen, F.H. Pollak and R.N. Sacks, Appl. Phys. Lett. 47, 891 (1985).
38. J. Menendez and M. Cardona, Phys. Rev. Lett. 51, 1297 (1983).
39. J. Menendez and M. Cardona, Phys. Rev. B31, 3696 (1985).

40. E. Anastassakis in Dynamic Properties of Solids, ed. by G. K. Horton and A.A. Maradudin (North Holland, N.Y. 1980) p. 157.
41. G.W. Rubloff, E. Anastassakis and F.H. Pollak, Solid State Comm. **13**, 1755 (1973).
42. D. E. Aspnes and A.A. Studna, Phys. Rev. **B27**, 985 (1983).
43. M.H. Grimsditch, D. Olego and M. Cardona, Phys. Rev. **B20**, 1758 (1979).
44. See, for example, M. Cardona in Light Scattering in Solids II, edited by M. Cardona (Springer, Heidelberg, 1982) p. 19 and references therein.
45. R. Trommer, G. Abstreiter and M. Cardona in Proc. Int. Conf. on Lattice Dynamics, Paris, 1977, ed. by . Balkanski (Flammarion, Paris, 1977) p. 189.
46. Our $C^2 n_i$ of Eq. (5) is equal to the quantity a_{Fi}^2 of Ref. 39. Therefore to evaluate C^2 from this reference we used a value of $n_i = 6 \times 10^{14} \text{ cm}^{-3}$ listed on p. 3697 for the liquid phase epitaxy sample.
47. Z. Hang, H. Shen and F.H. Pollak, J. Appl. Phys. **64**, 3233 (1988).
48. H. Shen and F.H. Pollak, Appl. Phys. Rev., **89**, 1638 (1974).
49. H. Shen, Z. Hang and F.H. Pollak, Proceedings of the Society of Photo Optical Instrumentation Engineers (SPIE, Bellingham, 1985) **524**, 118 (1985).
50. D.J. Stirland, and B. W. Staughan, Thin Solid Films, **31**, 139 (1976).
51. A. Karpol and B. Pratt, Solid State Comm. **12**, 325 (1973).
52. T.M. Donovan, E.J. Asheley, and H.C. Bennett, J. Opt. Soc. Am. **53**, 1403 (1963).
53. C. E. Jones and A. R. Hilton, J. Electrochem. Soc. **112**, 908 (1965).
54. P.J. Zansucchi and M.T. Duffy, Appl. Opt. **117**, 3477 (1978).
55. M.P. Lisitsa, V.N. Malinko, E. kV. Pidisnyi and G.E. Tsebulya, Surface Science, **11**, 411 (1986).
56. R.M. Silva, F.D. Orazio, Jr. and J.M. Bennett, Semicond. Int. **81**, (July, 1986).
57. H. Kuwamoto, D.E. Holmes and N. Otsuka, J. Electrochem. Soc. **134**, 1579 (1987).
58. D.J. Evans and S. Ushioda, Phys. Rev., **89**, 1638 (1974).
59. R. Carles, N. Saint-Cricq, A. Zwick, M.A. Renucci and J.B. Renucci, J. Phys. Soc. Japan, **49**, Suppl. A, 665 (1980).

60. F. Cerdeira, C.J. Buchenauer, F.H. Pollak and M. Cardona, *Phys. Rev.* B5, 580 (1971).
61. See for example, F.H. Pollak, *Suf. Sci.*, 37, 863 (1973).
62. G.P. Schwartz, G.J. Gualtieri, L.H. Dubois, L.H. and W.A. Bonner, *J. Electrochem. Soc.*, 131, 1716 (1984).
63. See, for example, R. Tsu, in Proceedings of the Society of Photo-Optical Instrumentation Engineers (SPIE, Bellingham, 1981) 276, 78 (1981) and reference therein.
64. J.P. Hirth and J. Lothe, Theory of Dislocations, 2nd edition (John Wiley and Son, New York, 1982) p.13.
65. P. Warekois, M.C. Levine and H.C. Gatos, *J. App. Phys.* 31, 1302 (1960).
66. A. Ksendozov, F.H. Pollak, P.M. Amirtharaj and J.A. Wilson, *J. Crystal Growth*, 86, 586 (1988).
67. See, for example, M. Cardona, in Modulation Spectroscopy (Academic Press, N.Y.T., 1969).
68. See, for example, Semiconductors and Semimetals Vol. 9, ed. by R.K. Willardson and A.C. Beer (Academic Press, N.Y. 1972).
69. See, for example, D.E. Aspnes in Handbook on Semiconductors, Vol. 2 ed. by T.S. Moss (North Holland, N.Y., 1980) p. 109 and references therein.
70. See, for example, F.H. Pollak in Proceedings of the Society of Photo-Optical Instrumentation Engineers (SPIE, Bellingham, 1981) 276, 142 (1981) and references therein.
71. R.N. Bhattacharya, H. Shen, P. Parayanthai, F.H. Pollak, T. Coutts and H. Aharoni, Proceedings of the Society of Photo-Optical Instrumentation Engineers 794, 81 (1987); also, *Phys. Rev.* B37, 4044 (1988).
72. R. Glosser and N. Bottka, Proceedings of the Society of Photo-Optical Instrumentation Engineers 794, 88 (1987).
73. P.M. Racciah, V. Lee, S. Ugar, D.Z. Xue, L.L. Abels and J.N. Garland, *J. Voc. Sci. Technol.* A3, 138 (1985).
74. P.M. Racciah, J.W. Garland, Z. Zhang, U. Lee, D.Z. Xue, L.L. Abels, S. Ugar and W. Wilensky, *Phys. Rev. Letts.* 53, 1958 (1984).
75. P.M. Racciah, J.W. Garland, Z. Zhang, L.L. Abels, S. Ugur, S. Mioc and M. Brown, *Phys. Rev. Letts.* 55, 1323 (1985).
76. P.M. Amirtharaj, .H. Dinan, J.J. Kennedy, P.R. Boyd and O.J. Glembocki, *J. Vac. Sci. Technol.* A4, 2028 (1986); see also, P.M. Amirtharaj, J.J. Kennedy and P.R. Boyd, to be published in *J. Vac. Sci. Technol.*

77. X.C. Shen, H. Shen, P. Parayanthal, F.H. Pollak, J.N. Schulman, A.L. Smirf, R.M. McFarlane and I. D'Haenens, Superlattices and Microstructures 2, 513 (1986).
78. F. H. Pollak in Photochemistry: Fundamental Processes and Measurement Techniques, ed. by W.L. Wallace, A.J. Nozik, S.K. Deb and R.H. Wilson (The Electrochemical Society, Pennington, 1982) p.608.
79. A. Ksendzov, F.H. Pollak, J.A. Wilson and V.A. Cotton, Appl. Phys. Letts. 49, 648 (1986).
80. P.M. Amirtharaj, K.K. Tiong, P. Parayanthal, F.H. Pollak and J.K. Furdyna, J. Vac. Sci. Technol. A3, 226 (1985).
81. We have subsequently determined that the principle of superposition can only be applied to the in-phase component of the PR signal. See H. Shen, F.H. Pollak, J.M. Woodall and R.N. Sacks, to be published in J. Vac. Sci. Technol.
82. G.H. Tsau, A. Shen, M. Madou, J.A. Wilson, V.A. Cotton and C.E. Jones, J. Appl. Phys. 59, 1238 (1986).
83. A. Ksendzov, F.H. Pollak, J.A. Wilson and V.A. Cotton, J. Crystal Growth 86, 834 (1988).
84. J.A. Wilson and V.A. Cotton, J. Vac. Sci. Technol. A3, 199 (1985).
85. W.F. Leonard and M. Michael, J. Appl. Phys. 50, 1450 (1979).
86. Y. Nemirovsky and I. Kidron, Solid State Electron. 22, 831 (1979).
87. M.A. Kinch, Semiconductors and Semimetals, Ed. by R.K. Willardson and A. Beer, Vol. 18 (Academic Press, New York, 1981), p.313.
88. R.B. Shoolar, B.K. Janousek, R.L. Alt, R.C. Carlscaen, M.J. Daugherty and A.A. Fote, J. Vac. Sci. and Technol. 21, 164 (1982).
89. E.H. Nicollian and A. Goetzberger, The Bell System Tech. Journal, 46, 1055 (1967).
90. R.F. DeKeersmaecker, D.J. DiMaria and S.T. Pantelides, The Physics of SiO₂ and Its Interfaces, Ed. S.T. Pantelides, (Pergamon Press, New York 1978) p. 189.

Table I Values of λ_1 , Γ_{01} , Γ_{t1} , λ_2 , Γ_{02} and Γ_{t2} at 300K for the $L0_1$ and $L0_2$ modes of the $Al_{0.48}In_{0.52}As/InP$ samples used in this study. Also listed are the 4K photoluminescence linewidths and the growth temperature, T_g .

Sample	T_s (°C)	LO ₁			LO ₂			PL Linewidth (meV)
		("AlAs-like" mode)			("InAs-like" mode)			
		λ_1 (Å)	Γ_{01} (cm ⁻¹)	Γ_{t1} (cm ⁻¹)	λ_2 (Å)	Γ_{02} (cm ⁻¹)	Γ_{t2} (cm ⁻¹)	
A	495	69(a)	2.8(a)	7.4	39(b)	4.9(b)	12.7	24
B	505	86(a)	2.8(a)	5.7	39(b)	3.3(b)	11.4	22
C	515	87(a)	2.8(a)	5.6	40(a)	2.8(a)	11.1	16
D	522	86(a)	2.8(a)	5.7	41(b)	4.0(b)	11.8	19
E	530	86(a)	2.8(a)	5.7	38(b)	3.3(b)	11.7	29
F	550	83(a)	2.8(a)	5.9	41(b)	5.0(b)	12.4	27

(a) One parameter SCH fit

(b) Two parameter SCH fit

TABLE

TABLE II. Values of $\Delta\omega_o$, $\Delta\Gamma_o$ and d_s for various polishing conditions on the $\langle 100 \rangle$ surface of GaAs and InP obtained from a least square fit of Eqs.(1)-(11) to the experimental data.

Polishing		conditions			
Material	Particle size (μm)	Time (min)	$\Delta\omega_o$ (cm^{-1}) ^a	$\Delta\Gamma_o$ (cm^{-1}) ^b	d_s (\AA) ^a
GaAs	0.05	2.5	$+8.0 \pm 0.5$	≤ 3.0	100 ± 25
	0.05	5.0	$+8.6 \pm 0.5$	≤ 3.0	120 ± 25
	0.05	10	$+8.6 \pm 0.5$	≤ 3.0	150 ± 25
	0.05	30	$+8.0 \pm 0.5$	≤ 3.0	178 ± 25
	0.05	60	$+9.1 \pm 0.5$	≤ 3.0	200 ± 25
	0.3	10	$+10.7 \pm 0.2$	≤ 3.0	235 ± 15
	0.3	15	$+10.5 \pm 0.5$	≤ 3.0	250 ± 30
	0.3	60	$+11.4 \pm 0.5$	≤ 3.0	360 ± 50
	1.0	2	$+10.4 \pm 0.5$	≤ 3.0	530 ± 75
InP	0.05	5	$+12.6 \pm 0.5$	≤ 3.0	190 ± 25
	0.05	10	$+12.1 \pm 0.5$	≤ 3.0	230 ± 15
	0.05	60	$+12.1 \pm 0.5$	≤ 3.0	300 ± 40
	0.3	10	$+12.3 \pm 0.3$	≤ 3.0	385 ± 30
	0.3	30	$+12.5 \pm 0.5$	≤ 3.0	440 ± 50
	0.3	60	$+12.5 \pm 0.5$	≤ 3.0	533 ± 40

a. Averages over the value obtained for the different laser excitation wavelengths

b. This range of $\Delta\Gamma_o$ produced no significant change in the fit to the experimental data.

TABLE III. Values of $\Delta\omega_o$, $\Delta\Gamma_o$, d_s for various polishing conditions on the $\langle 111 \rangle$ surface of GaAs and InP obtain from a least-square fit of Eqs.(1)-(11) to the experimental data.

Polish conditions					
Material	Particle size (μm)	Time (min)	$\Delta\omega_o$ (cm^{-1}) ^a	$\Delta\Gamma_o$ (cm^{-1})	d_s (\AA) ^a
GaAs	0.05	2.5	$+1.3 \pm 0.5$	5.5 ± 1.0	100 ± 50
	0.05	5	$+1.4 \pm 0.5$	6.2 ± 1.0	200 ± 100
	0.05	10	$+1.3 \pm 0.5$	6.5 ± 1.0	340 ± 100
	0.05	30	$+1.5 \pm 0.5$	7.0 ± 1.0	400 ± 100
	0.05	60	$+1.5 \pm 0.5$	7.3 ± 1.0	440 ± 100
	0.3	10	$+1.0 \pm 0.2$	5.5 ± 1.0	1200 ± 200
	0.3	60	$+1.4 \pm 0.5$	6.3 ± 1.0	4500 ± 500
InP	0.05	10	$+2.8 \pm 1.0$	4.8 ± 1.0	350 ± 100
	0.05	60	$+3.3 \pm 1.0$	7.0 ± 1.0	1100 ± 200
	0.3	10	$+3.6 \pm 1.0$	6.0 ± 1.0	3400 ± 500
	0.3	60	$+3.6 \pm 1.0$	7.0 ± 1.0	4500 ± 500

a. Self-consistent fit to data for all five laser wavelengths.

Table IV. Values of the energy gap, E_1 , and broadening parameter, Γ_1 , at 77K for several $\text{Hg}_{1-x}\text{Cd}_x\text{Te}$ samples.

Sample	E_1 (eV)	Γ_1 (meV)
LPE- $\text{Hg}_{0.78}\text{Cd}_{0.22}\text{Te}$ (n-type)	$\begin{cases} 2.43^{(a)} \\ 2.40^{(b)} \end{cases}$	$\begin{matrix} 96^{(a)} \\ 110^{(b)} \end{matrix}$
MBE- $\text{Hg}_{0.86}\text{Cd}_{0.14}\text{Te}$ (n-type)	$2.36^{(b)}$	$94^{(b)}$
Bulk- $\text{Hg}_{0.7}\text{Cd}_{0.3}\text{Te}$ (n-type)	$2.49^{(b)}$	$146^{(b)}$
Bulk- $\text{Hg}_{0.7}\text{Cd}_{0.3}\text{Te}$ (p-type)	$\begin{cases} 2.50^{(b)} \\ 2.53^{(c)} \end{cases}$	$\begin{matrix} 79^{(b)} \\ 78^{(c)} \end{matrix}$

- (a) 3.39 μm pump measurement
(b) 4067A pump measurement
(c) 4579A pump measurement

Table V. - Values of the time constant τ at 77K for several $\text{Hg}_{1-x}\text{Cd}_x\text{Te}$ samples.

Sample	τ (10^{-3} sec)
LPE- $\text{Hg}_{0.78}\text{Cd}_{0.22}\text{Te}$ (n-type)	$\begin{cases} 4.4 \pm 1^{(a)} \\ 2.8 \pm 0.5^{(b)} \end{cases}$
Bulk- $\text{Hg}_{0.7}\text{Cd}_{0.3}\text{Te}$ (p-type)	$1.7 \pm 0.3^{(b)}$

(a) 3.39 μm pump measurement

(b) 4067A pump measurement

FIGURE CAPTIONS

- Fig. 1. Raman spectrum of $\text{Al}_{0.48}\text{In}_{0.52}\text{As}/\text{InP}$ sample C.
- Fig. 2. Experimental data (dotted line) for LO_2 and LO_1 for three $\text{Al}_{0.48}\text{In}_{0.52}\text{As}/\text{InP}$ samples and SCM fits for one parameter (solid line) and two parameter (dashed line) cases.
- Fig. 3. Photoluminescence linewidth of several $\text{Al}_{0.48}\text{In}_{0.52}\text{As}/\text{InP}$ samples as a function of substrate temperature, T_s .
- Fig. 4. Experimental data (dotted line) for LO_2 and LO_1 for three $\text{Al}_{0.48}\text{In}_{0.52}\text{As}/\text{InP}$ samples and Fano model fit (solid line). The values of the Fano parameters Q_F and Γ_F for the various modes are given.
- Fig. 5. Relationship between width Γ and asymmetry of the Raman line in (a) $\mu\text{c-Si}$ and (b) $\mu\text{c-Ge}$, corrected by instrumental resolution. The points correspond to samples prepared by molecular beam deposition.
- Fig. 6. (a) Electron diffraction pattern and (b) TEM micrograph for a $\mu\text{c-Ge}$ film.
- Fig. 7. (a) Electrical conductivity and (b) Raman measurements for molecular beam deposition $\mu\text{c-Si}$ as a function of annealing temperatures.
- Fig. 8. (a) Electrical conductivity and (b) Raman measurements for molecular beam deposition $\mu\text{c-Ge}$ as a function of annealing temperatures.
- Fig. 9. Raman scattering at 4579A from the $\langle 100 \rangle$ surface of n-GaAs sample 782-8A for the configuration $x(y,z)\bar{x}$.
- Fig. 10. The intensity ratios I_2/I_1 , I_3/I_1 and I_4/I_1 at 4579A as a function of impurity concentration n_i .
- Fig. 11 (a) Raman spectra of $\langle 100 \rangle$ InP at 5145 A. Spectrum A is from on undamaged surface. Spectra B, C and D are from damaged surfaces which were polished with 0.05 μm particle size for 5, 10, 60 min., respectively. (b) Raman spectra of $\langle 100 \rangle$ GaAs at 5145 A. Spectrum A is from on undamaged surface. Spectra B,C and D are from damaged surfaces which were polished with 0.05 μm particle size for 5, 10, 60 min., respectively.

- Fig. 12 (a) Raman scattering from $\langle 100 \rangle$ InP: undamaged surface at 5145A (spectrum A) and material damaged with 0.05 μm particle size for 5 min. at 5145, 5017, 4880, 4765 and 4579 A (spectra B-F). (b) Raman scattering from $\langle 100 \rangle$ GaAs: undamaged surface 5145 A (spectrum A) and material damaged with 0.3 μm particle size for 60 min. at 5145, 5017, 4880, 4765 and 4579 A (spectra B-F).
- Fig. 13. (a) Raman scattering from $\langle 111 \rangle$ InP: undamaged surface at 5145 A (spectrum A) and material damaged with 0.05 μm particle size for 10 minutes at 5145, 4880 and 4579 A (spectra B-D). (b) Raman scattering from $\langle 111 \rangle$ GaAs: undamaged surface at 5145 A (spectrum A) and material damaged with 0.3 μm particle size for 10 minutes at 5145, 4880 and 4579 A (spectra B-D).
- Fig. 14. (a) For $\langle 111 \rangle$ InP the variation in LO-phonon linewidth Γ (deconvoluted) and peak shift $\Delta\omega$ as a function of optical skin depth, d_o , for the undamaged case and material damaged under various polishing conditions. (b) For $\langle 111 \rangle$ GaAs the variation in LO-phonon linewidth Γ (deconvoluted) and peak shift $\Delta\omega$ as a function of optical skin depth, d_o , for the undamaged case and material damaged under various polishing conditions.
- Fig. 15. (a) Comparison of experiment and fit for $\langle 100 \rangle$ InP damaged with 0.3 μm particle size for 10 min. at 5145 and 4880 A excitation lines. (b) Comparison of experiment and fit for $\langle 100 \rangle$ GaAs damaged with 0.3 μm particle size for 10 min. at 5145 and 4880 A excitation lines.
- Fig. 16. Damage skin depth $d_s(t)$ versus time for GaAs $\langle 100 \rangle$ damaged with 0.05 μm grit. The open circles are experimental results from Table II. The solid and dotted lines represent $d_s^{\text{eff}}(t)$ versus time using $d_m = 200\text{\AA}$ and $d_m = 175\text{\AA}$, respectively, for the least square fit comparison.
- Fig. 17. The damaged skin depth $d_s(t)$ versus time for GaAs $\langle 111 \rangle$ damaged with 0.05 μm grit. The open circles are experimental results from Table III. The solid and dotted lines represent $d_s^{\text{eff}}(t)$ versus time using $d_m = 200\text{\AA}$ and $d_m = 400\text{\AA}$, respectively, for the least fit comparison.
- Fig. 18. Zincblende structure in the $\langle 100 \rangle$ direction. The distance between the layers in $(1/4) \underline{a}$, where \underline{a} is the lattice constant.

- Fig. 19. Zincblende structure in the $\langle 111 \rangle$ direction. The distance between the n and $n+1$ layers is $3/12 a$ and the distance between the $n+1$ and $n+2$ layers is $(3/4)a$.
- Fig. 20. Least-square fit of Eq. (1a) to $f(x; 2.5 \text{ min.}, 200\text{\AA})$ for $\langle 100 \rangle$ GaAs. The solid line is $f(x; 2.5 \text{ min.}, 200\text{\AA})$ and dotted line is the exponential form.
- Fig. 21. Least square fit of Eq. (9) to $f(x; 2.5 \text{ min.}, 440\text{\AA})$ for $\langle 111 \rangle$ GaAs. The solid line is $f(x; 2.5 \text{ min.}, 440\text{\AA})$ and dotted line is the exponential form.
- Fig. 22. Photoreflectance spectrum from the LPE-Hg_{0.78}Cd_{0.22}Te (n-type) sample (solid line) at 77K in the vicinity of the E_1 transition using 3.39 μm pump. The dashed line is a fit to Eq. (30).
- Fig. 23. Frequency dependence of the photoreflectance intensity (3.39 μm pump) of sample LPE-Hg_{0.78}Cd_{0.22}Te. The solid line is a fit to Eq. (34).
- Fig. 24. Photoreflectance spectra from the LPE-Hg_{0.78}Cd_{0.22}Te (n-type) sample (dotted curves at 77K using the 4067\text{\AA} pump for modulation frequencies of 103 Hz, 600 Hz and 4035 Hz. The solid lines are fit to Eq. (30).
- Fig. 25. Frequency dependence of the photoreflectance intensity (4067\text{\AA} pump) of sample LPE-Hg_{0.78}Cd_{0.22}Te. The solid line is a fit to Eq. (5).
- Fig. 26. Photoreflectance spectrum from the MBE-Hg_{0.86}Cd_{0.14}Te sample (dotted curve) at 77K using the 4067\text{\AA} pump. The solid line is a fit to Eq. (30).
- Fig. 27. Photoreflectance spectrum from the bulk-Hg_{0.7}Cd_{0.3}Te (n-type) sample (dotted curves) at 77K using the 4067\text{\AA} pump. The solid lines are fits to Eq. (30).
- Fig. 28. Photoreflectance spectra from the bulk-Hg_{0.7}Cd_{0.3}Te (p-type) sample (dotted curves) at 77K using the 4067\text{\AA} pump for frequencies of 84 Hz, 641 Hz and 3215 Hz. The solid lines are fits to Eq. (30).
- Fig. 29. Photoreflectance spectrum from the bulk Hg_{0.7}Cd_{0.3}Te (p-type) sample at 77K using the 4579\text{\AA} pump. The solid line is a fit to Eq. (30).

- Fig. 30. Frequency dependence of the photoreflectance intensity (4067A pump) of sample bulk- $\text{Hg}_{0.7}\text{Cd}_{0.3}\text{Te}$ (p-type). The solid line is a fit to Eq. (34).
- Fig. 31. Capacitance-voltage curves at 77K for different time exposures of 2800A light at zero bias.
- Fig. 32. Photo-induced flatband shift, ΔU_{fb} , as a function of the total number of photons per cm^2 , P , for light of wavelength 3300A, 2800A and 2200A. The inset shows an expanded version of the 2800A results. The solid lines are a least-squares fit to Eqs. (39)-(41) and (44).
- Fig. 33. Capacitance-voltage curves at 77K for (1) no light exposure, (2) after exposure to 1 μm light for one hour and a bias of +10 V and (3) 10 minutes after the light and bias were shut off.
- Fig. 34. Proposed model of the $\text{Hg}_{0.7}\text{Cd}_{0.3}\text{Te}(\text{n-type})/\text{SiO}_2\text{-Photox}^{\text{TM}}$ interfacial region including a distribution of electron traps in the SiO_2 centered around E_o with full-width at half-maximum of δE_o . For the sake of clarity the energy gaps of the $\text{Hg}_{0.7}\text{Cd}_{0.3}\text{Te}$ (~250 meV) and SiO_2 (~9 eV) are not drawn to scale. The dark region represents the states per unit area accessed by the charging only process while the shaded region indicates the region of charging and discharging.
- Fig. 35. Experimental (open circles) and theoretical (closed circles) values of $n_s(h\nu)$.

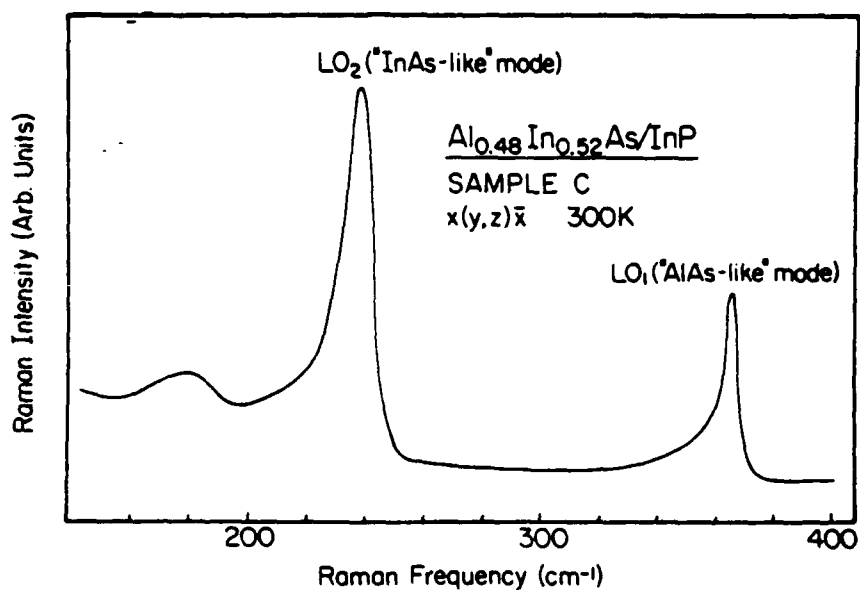


FIG. 1

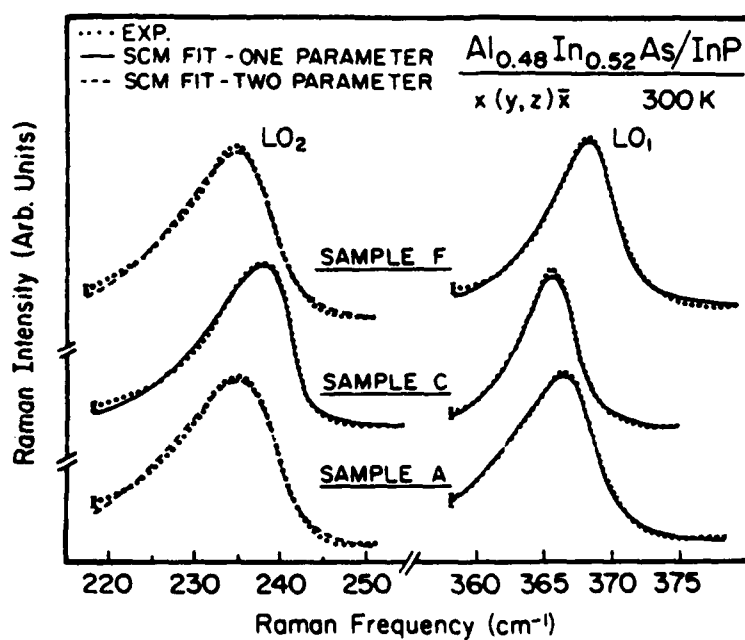


FIG. 2

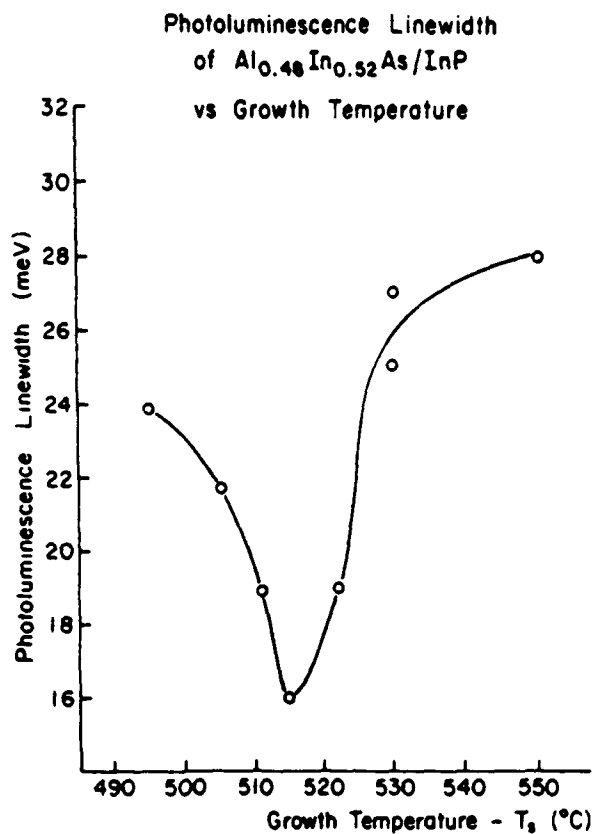


FIG. 3

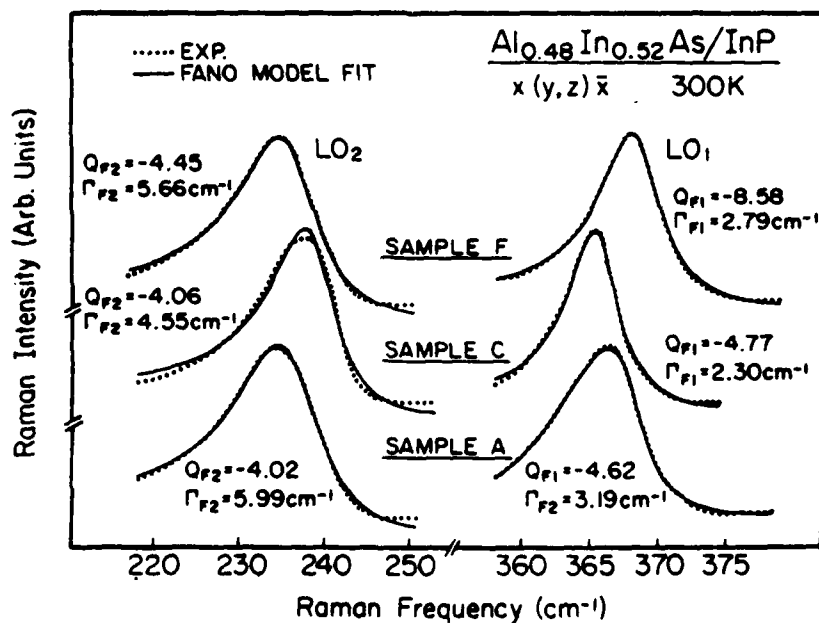


FIG. 4

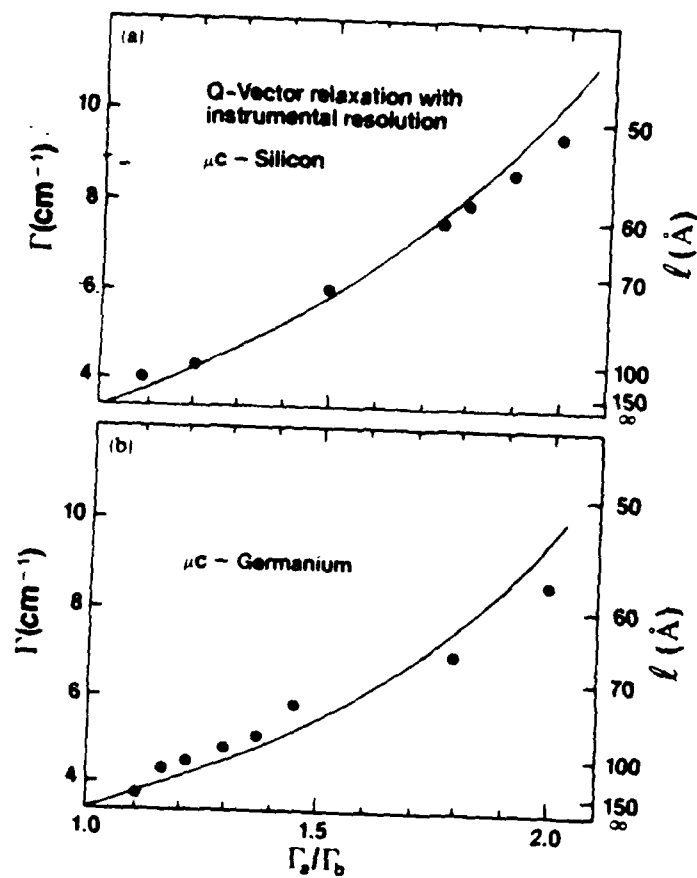


FIG. 5

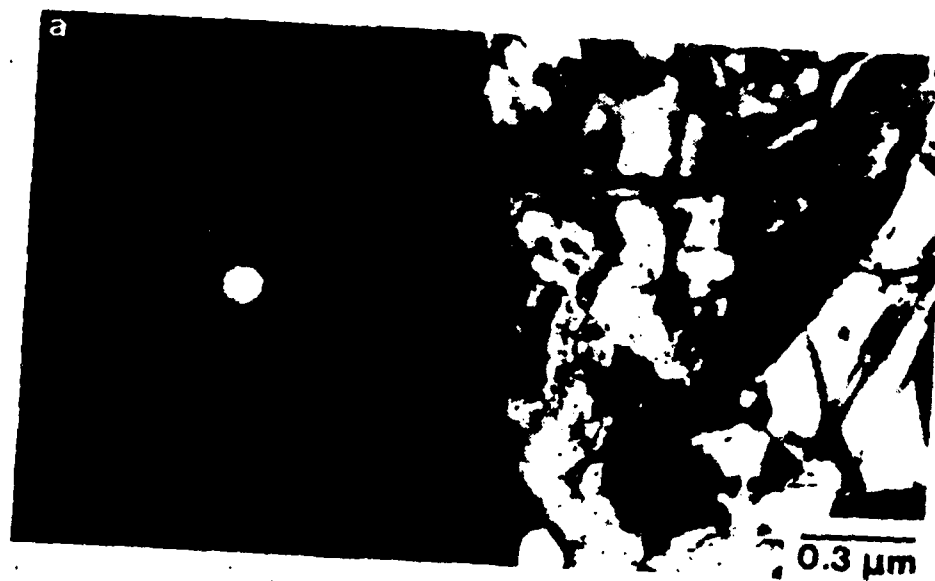


FIG. 6

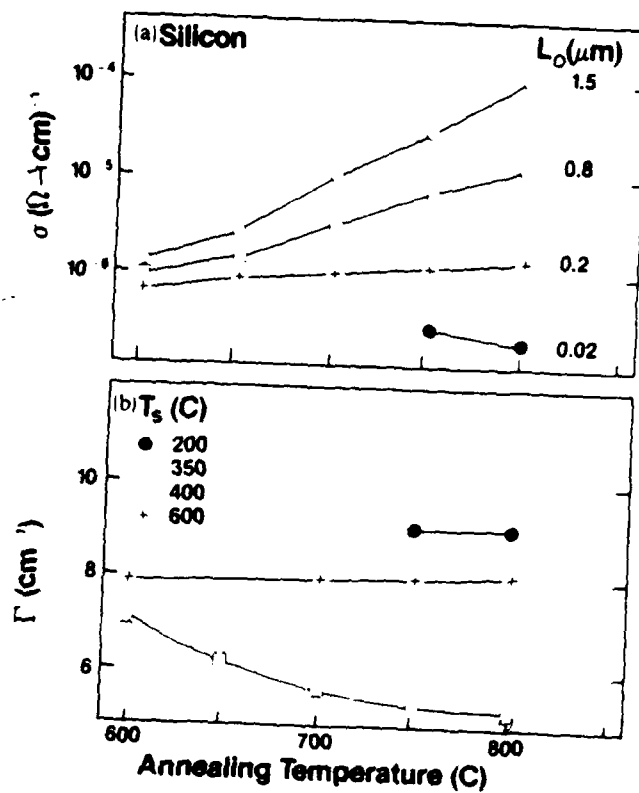


FIG. 7

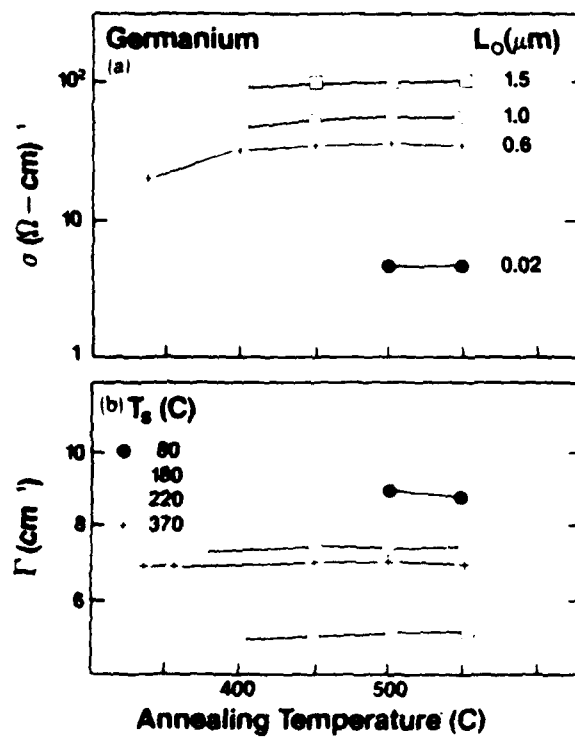


FIG. 8

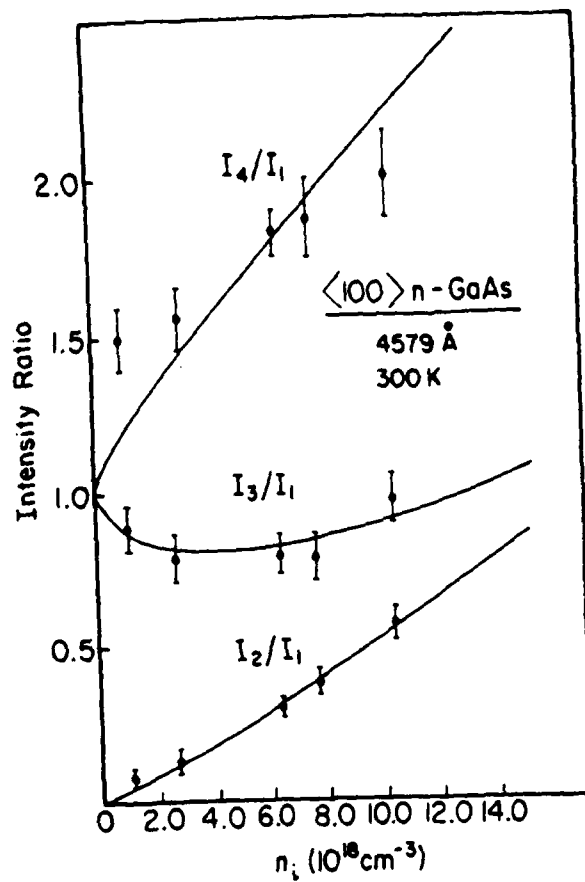


FIG. 9

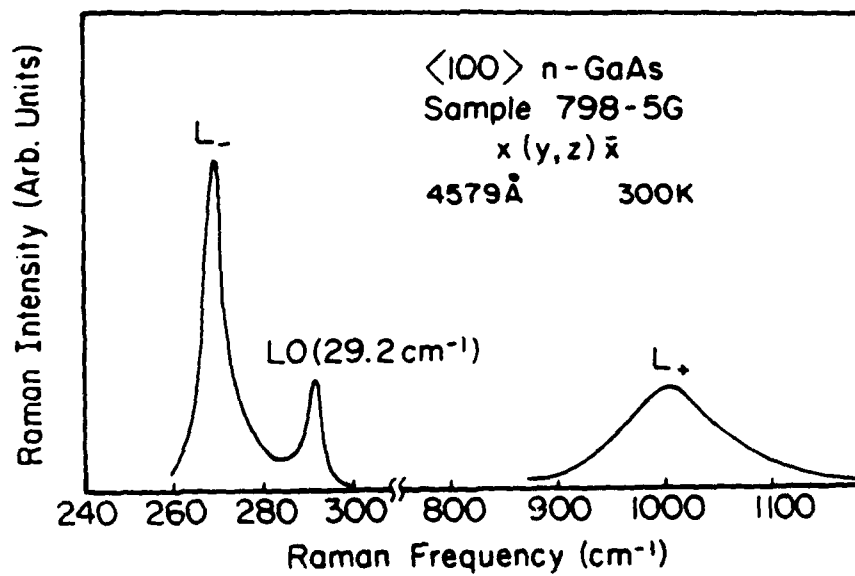


FIG. 10

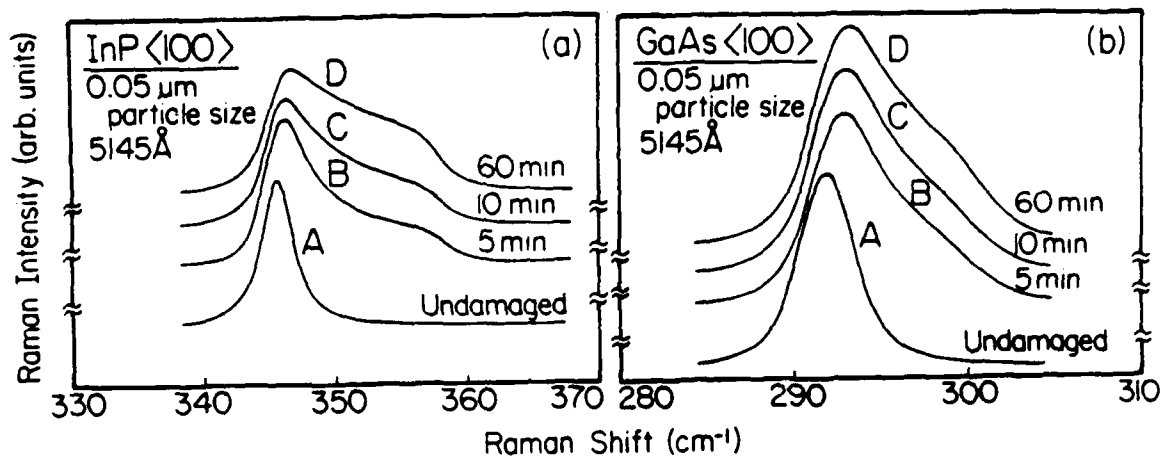


FIG. 11

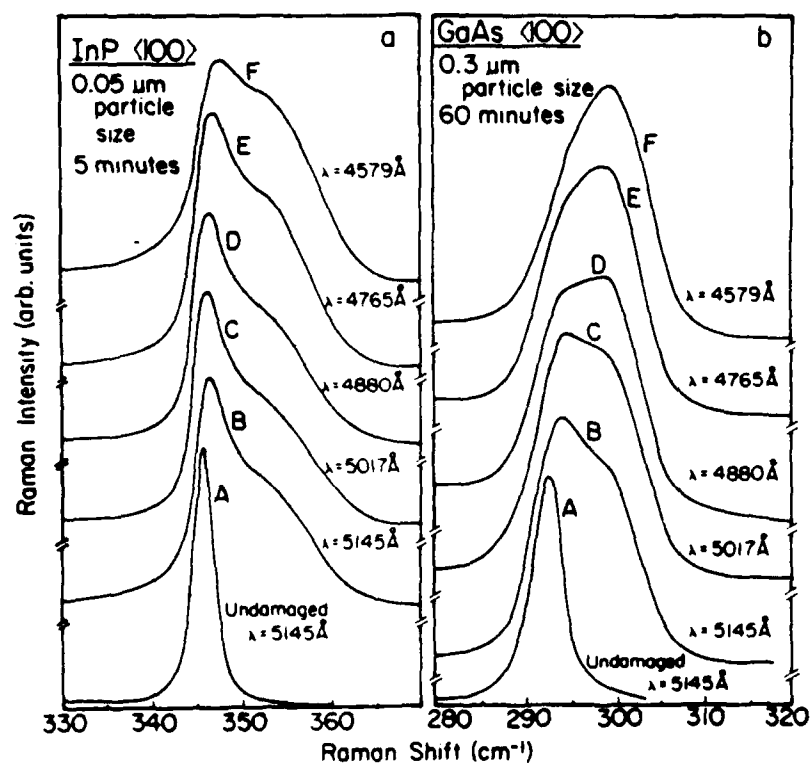


FIG. 12

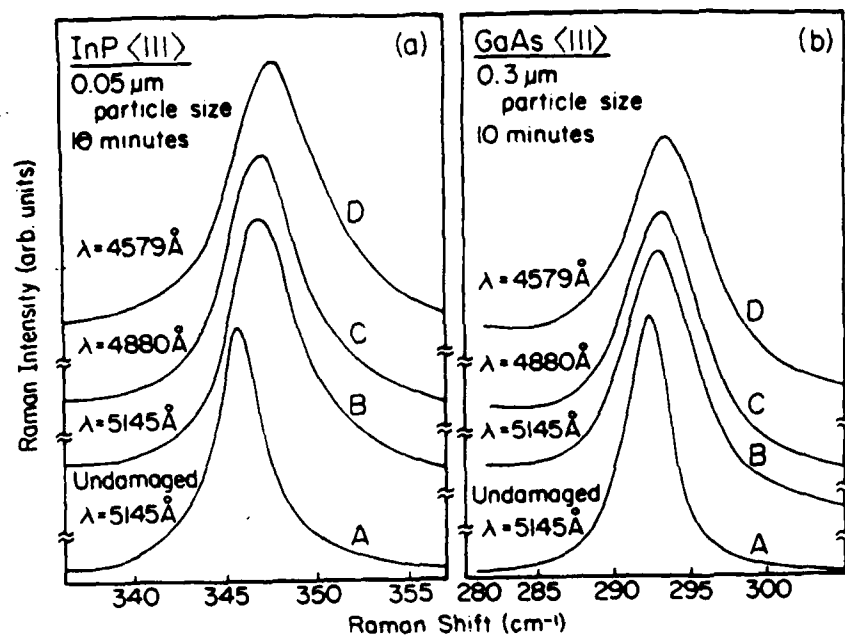


FIG. 13

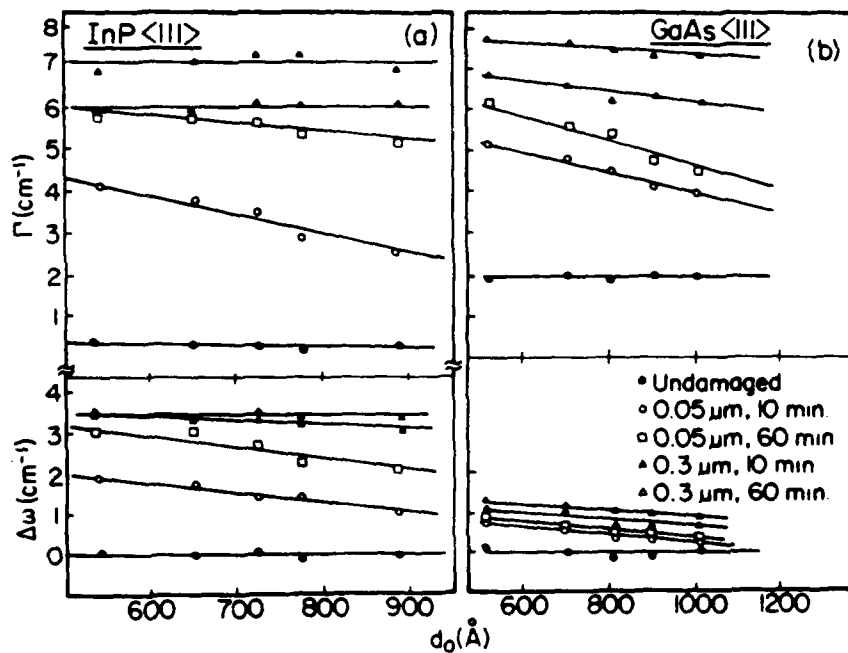


FIG. 14

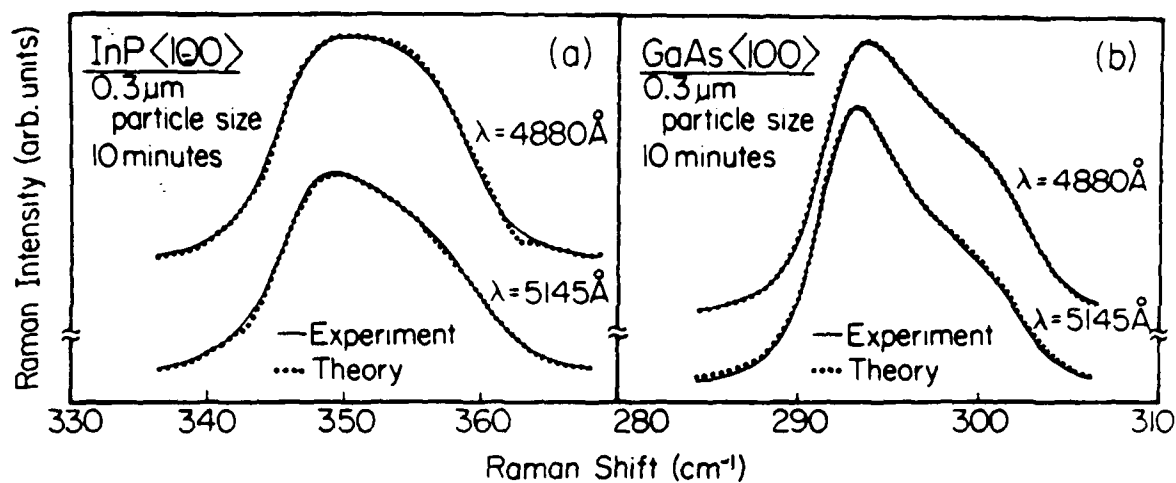


FIG. 15

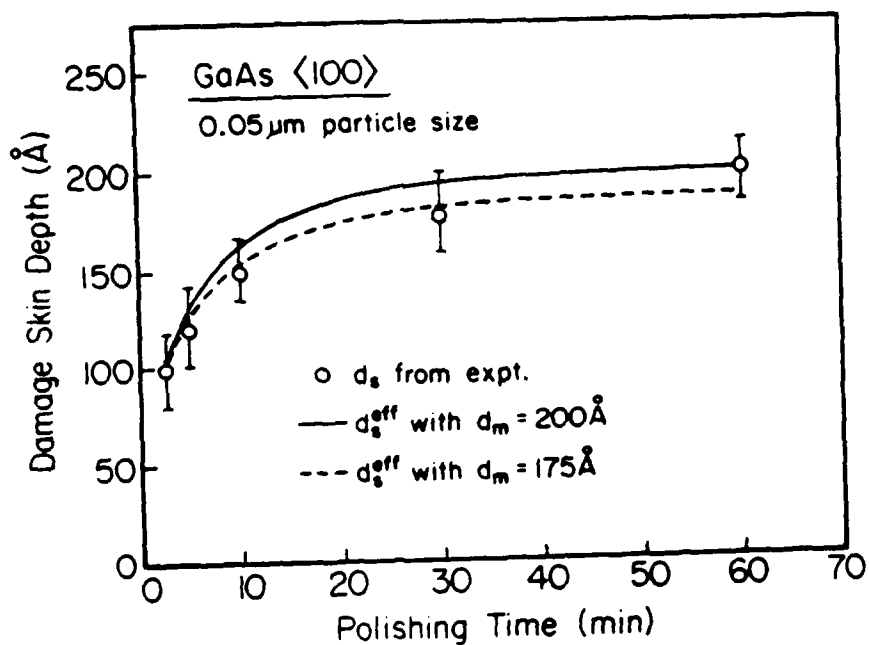


FIG. 16

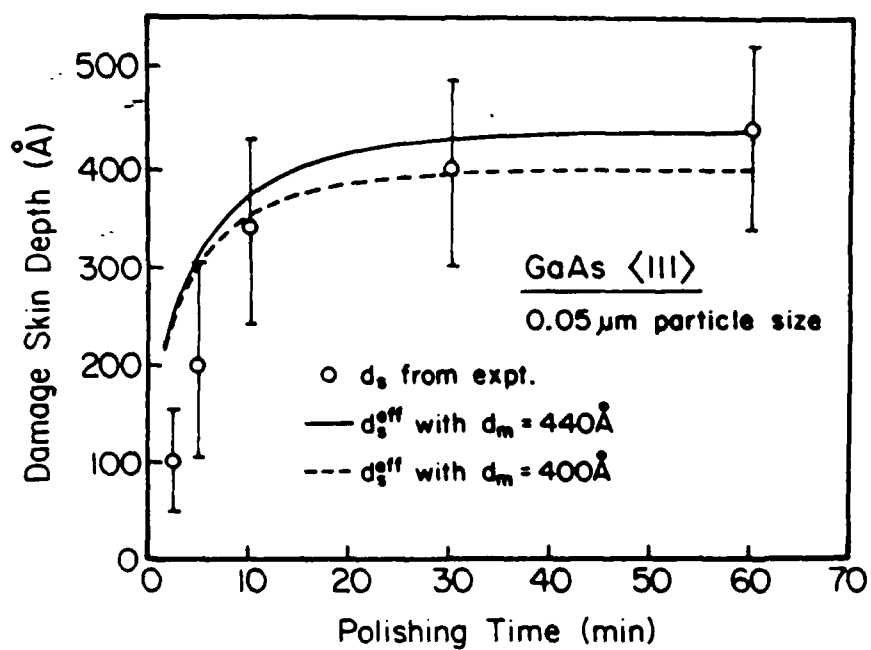


FIG. 17

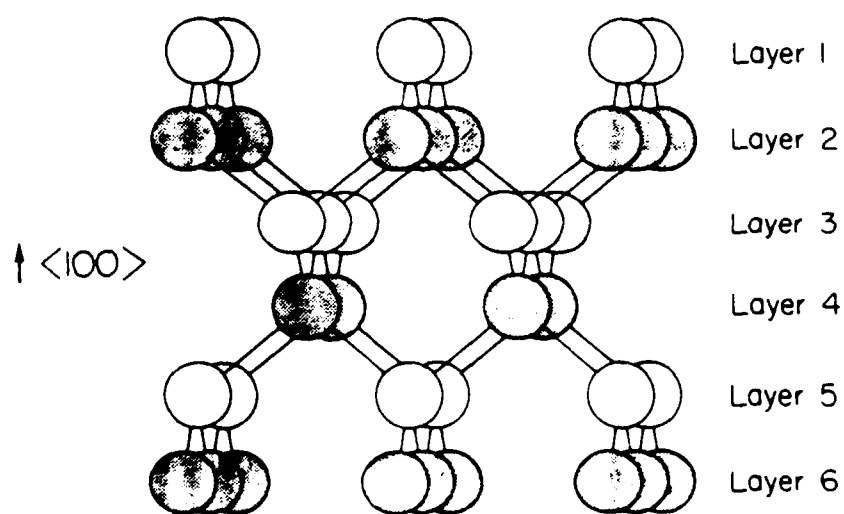


FIG. 18

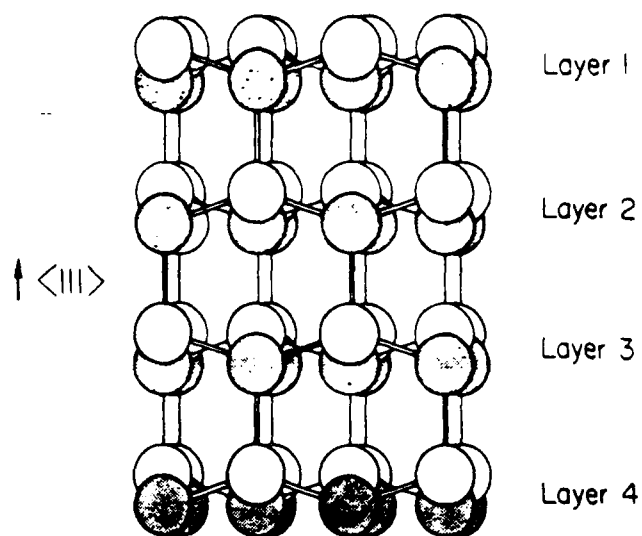


FIG. 19

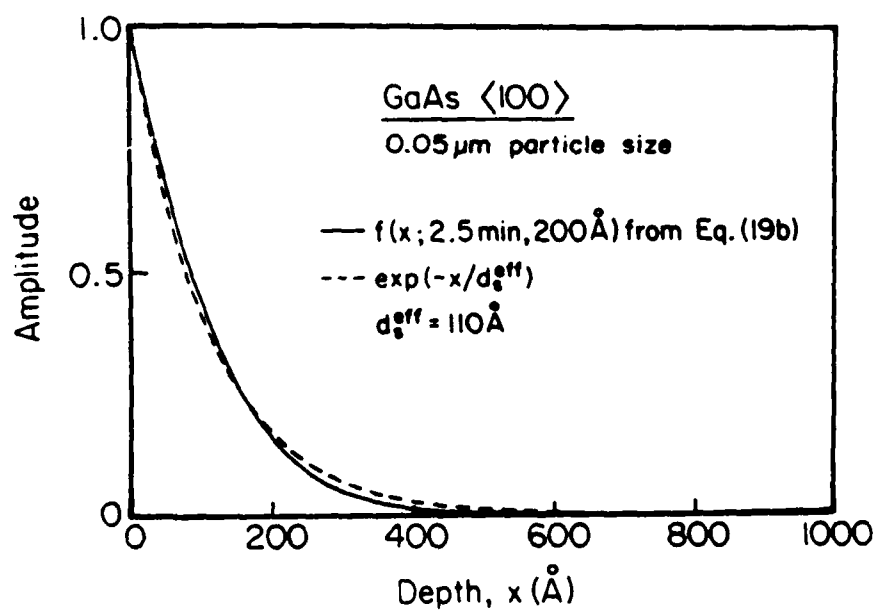


FIG. 20

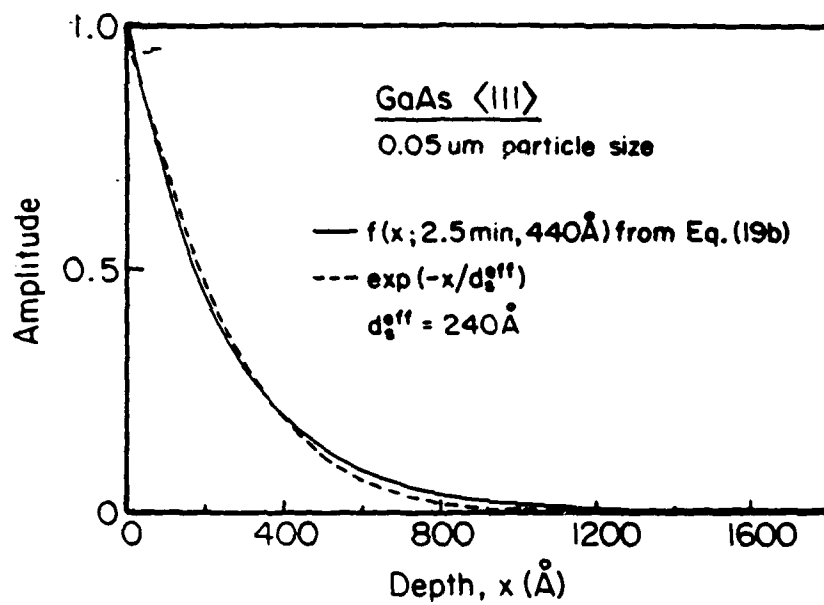


FIG. 21

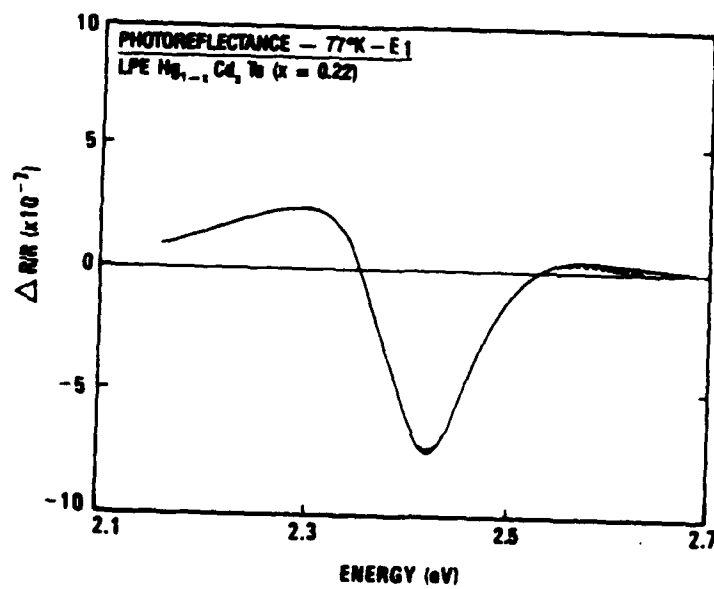


FIG. 22

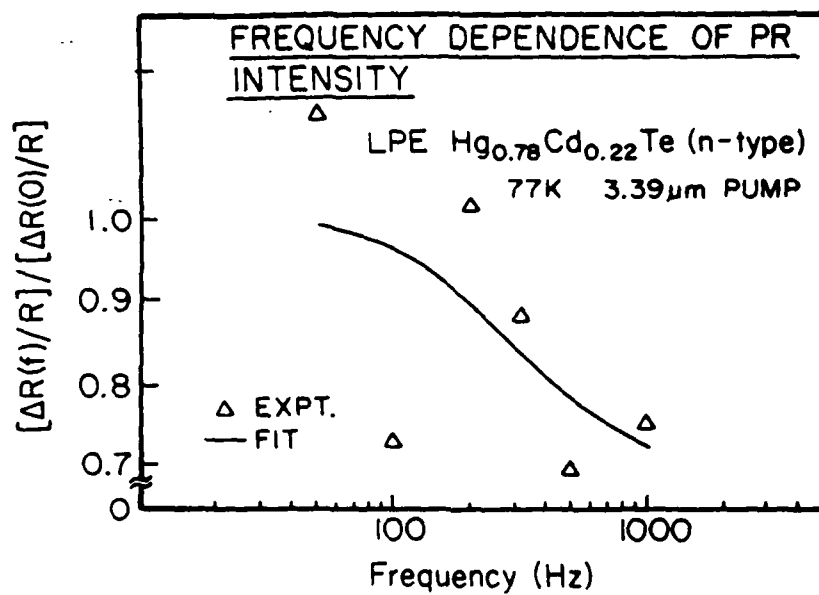


FIG. 23

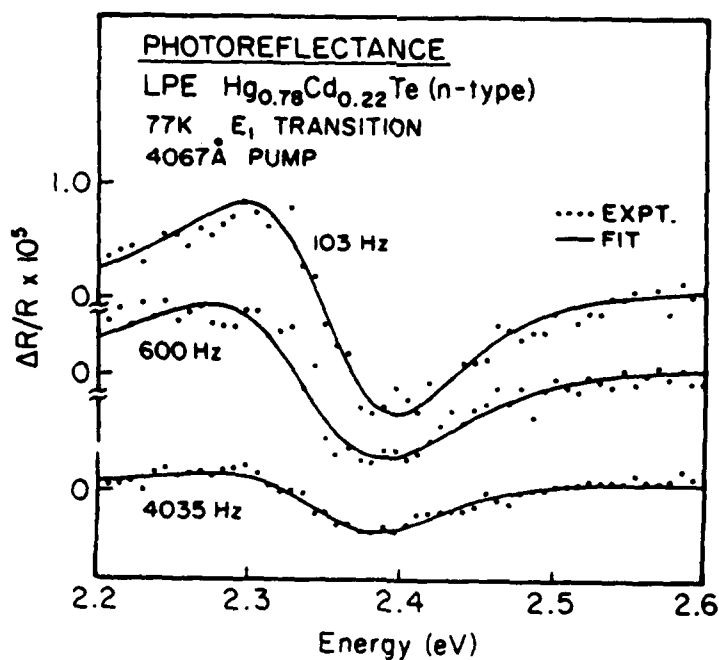


FIG. 24

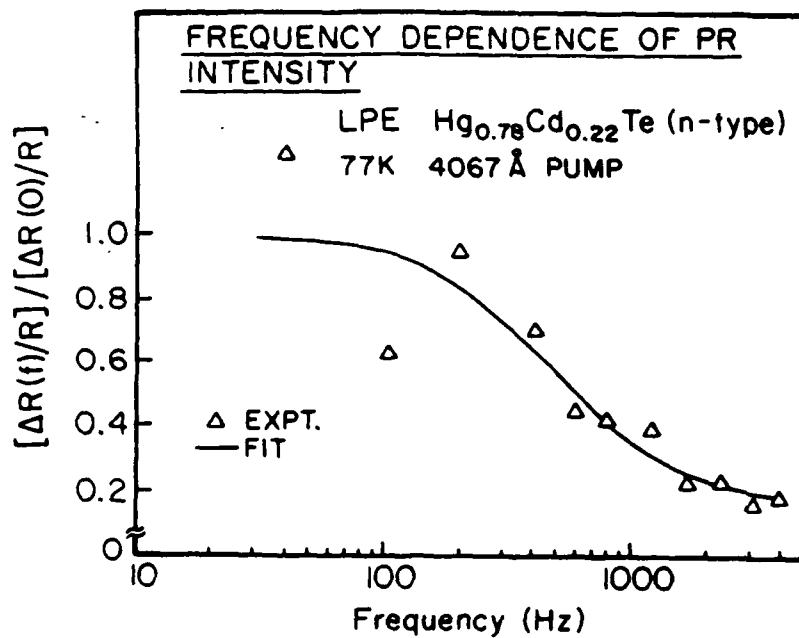


FIG. 25

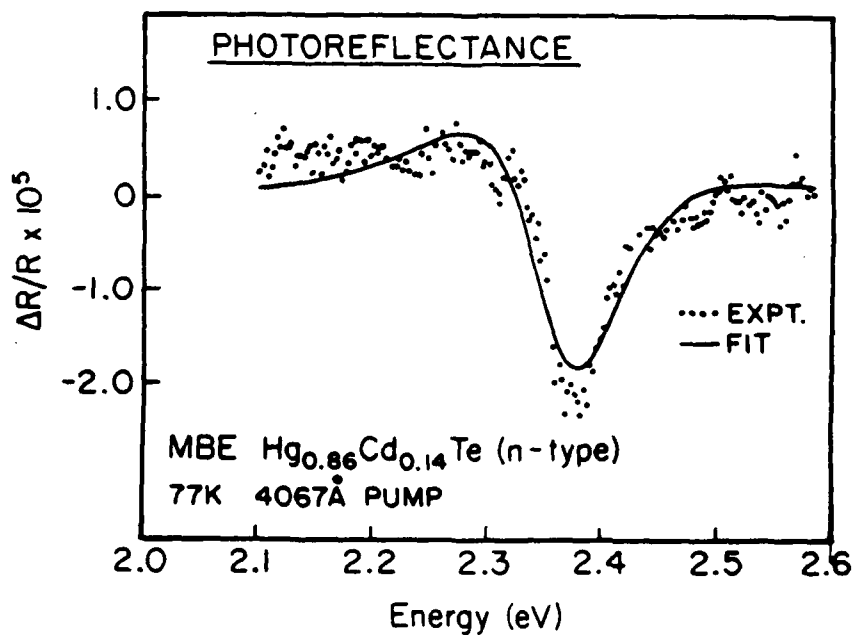


FIG. 26

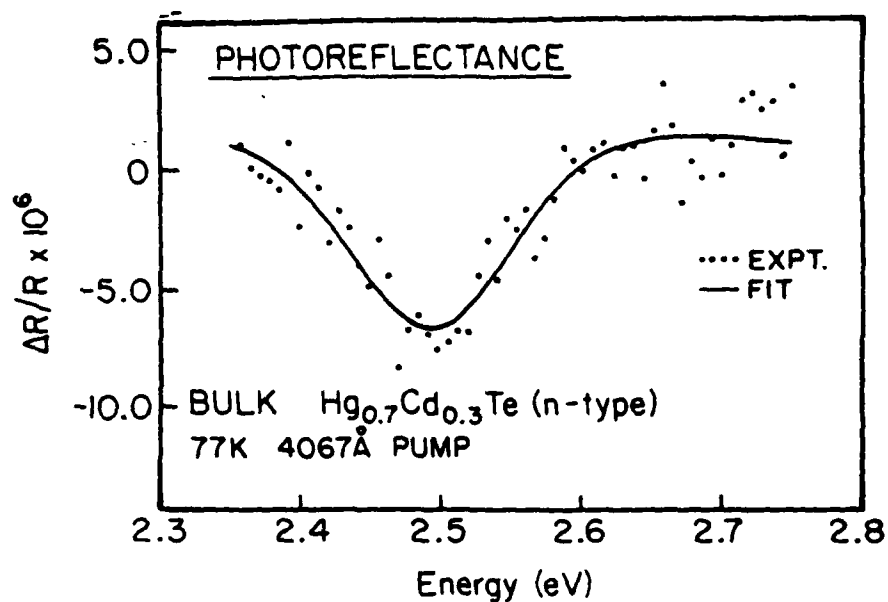


FIG. 27

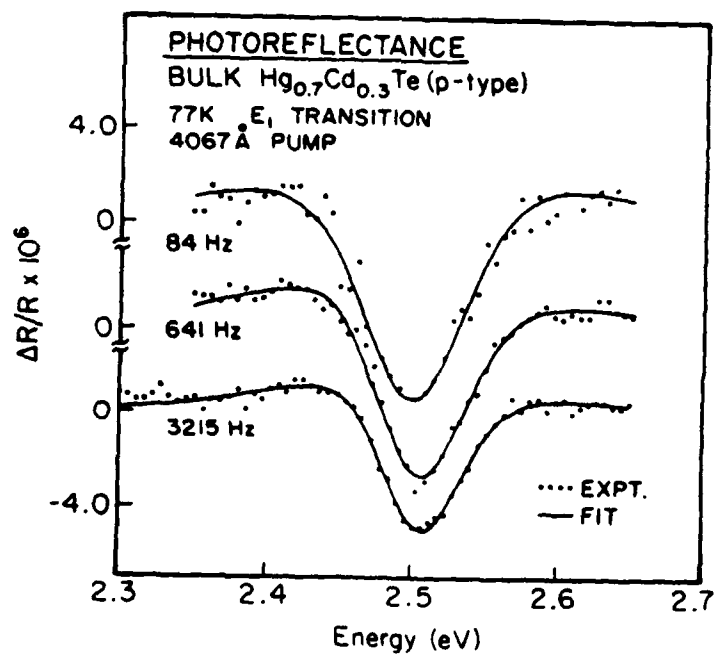


FIG. 28

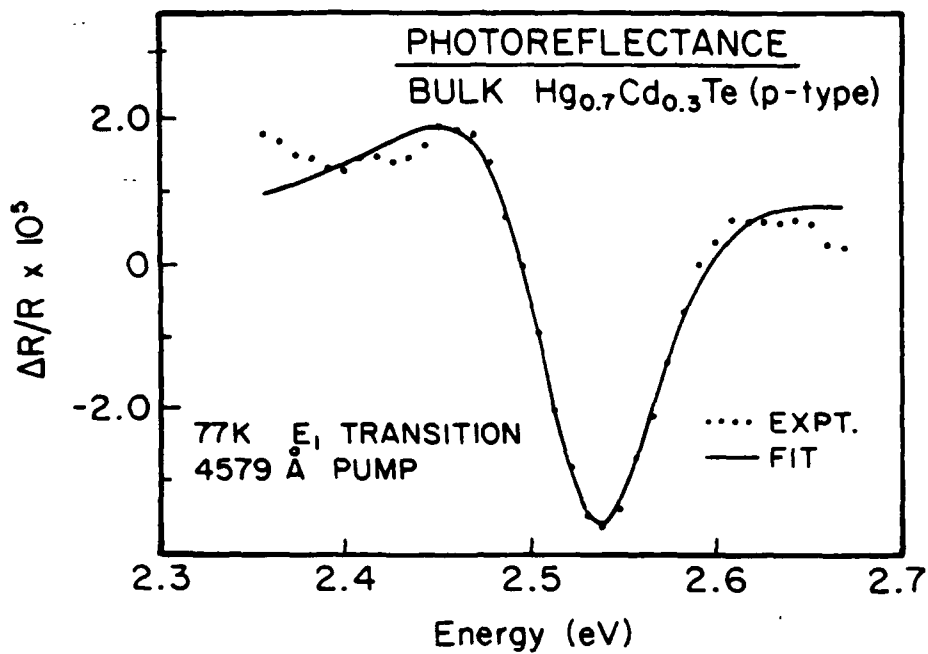


FIG. 29

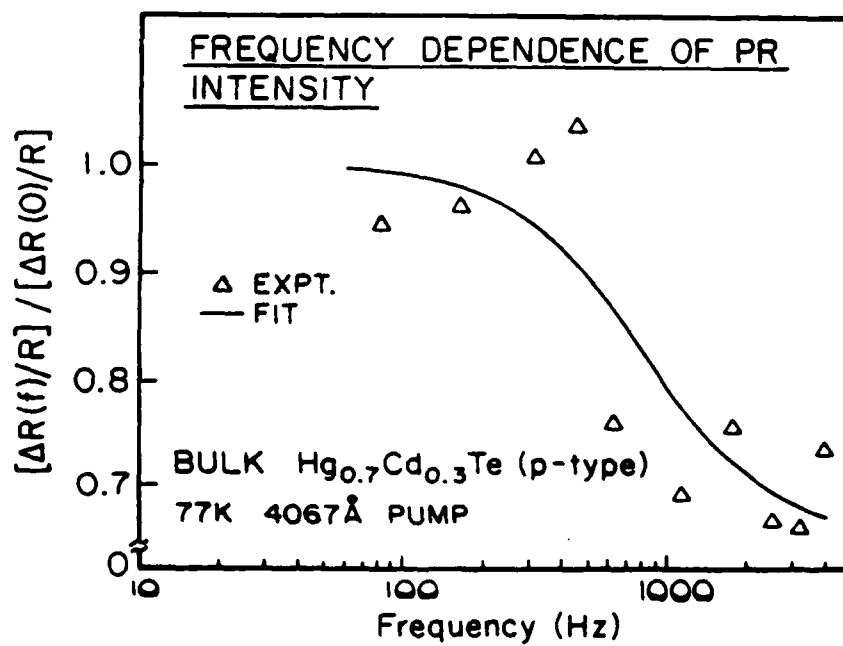


FIG. 30

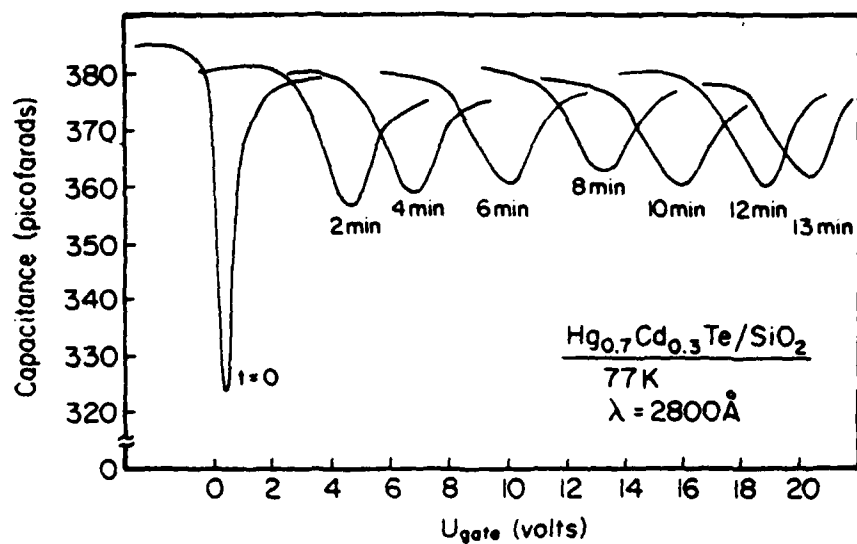


FIG. 31

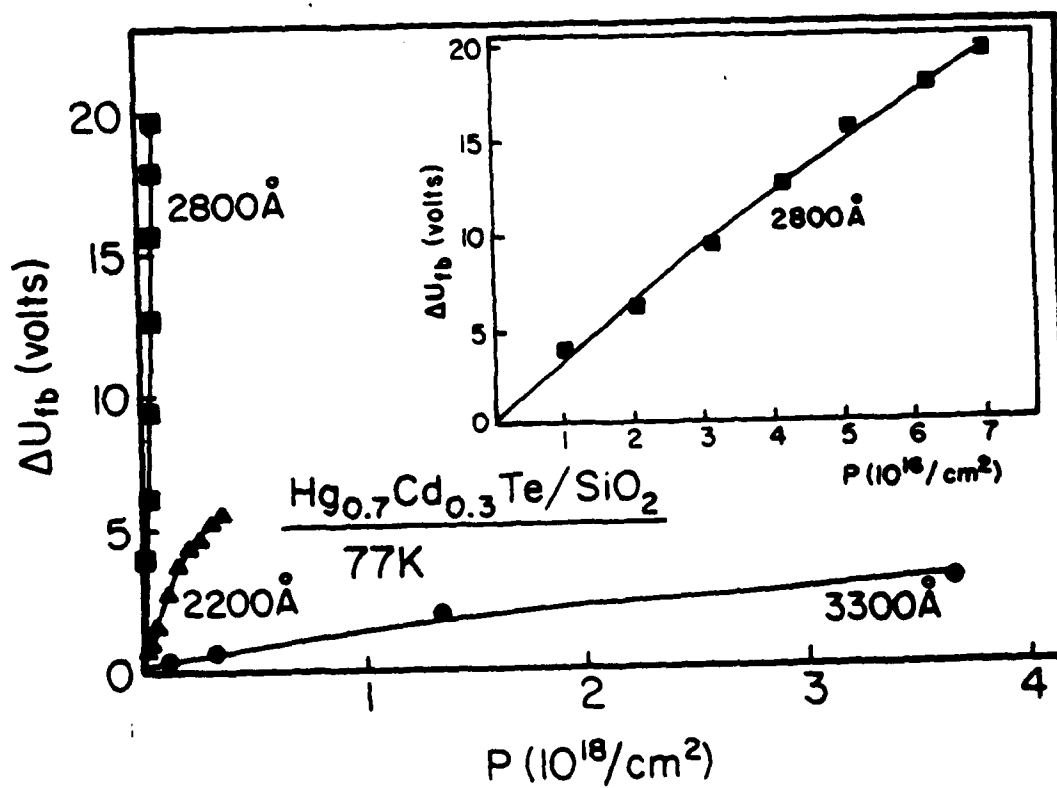


FIG. 32

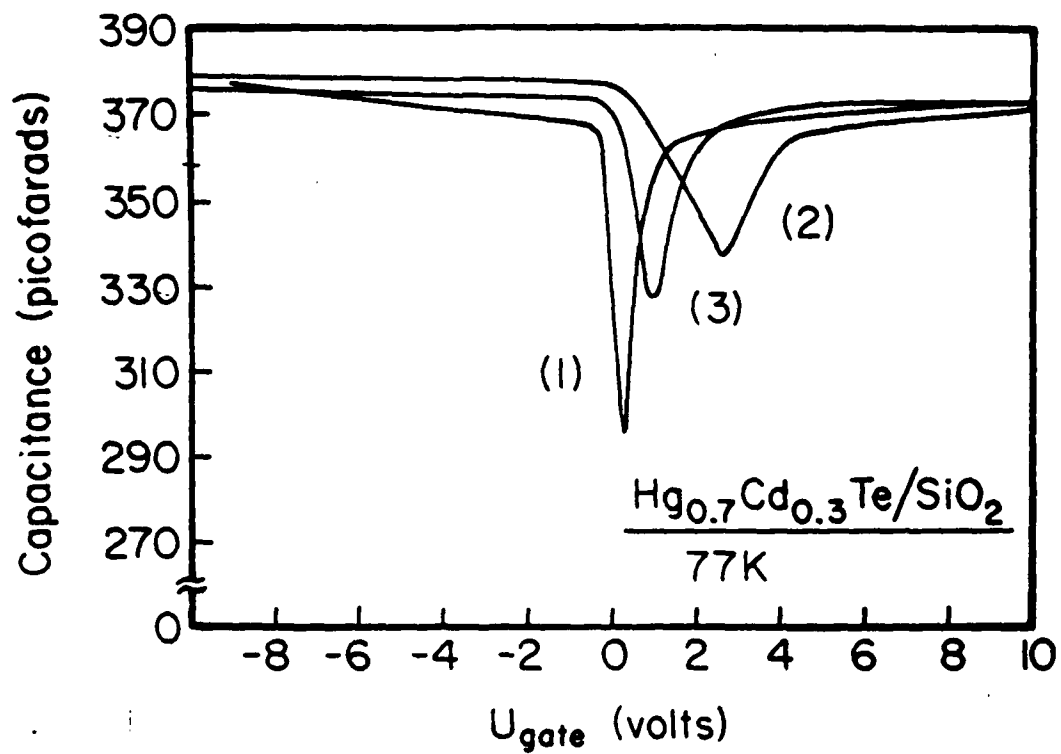


FIG. 33

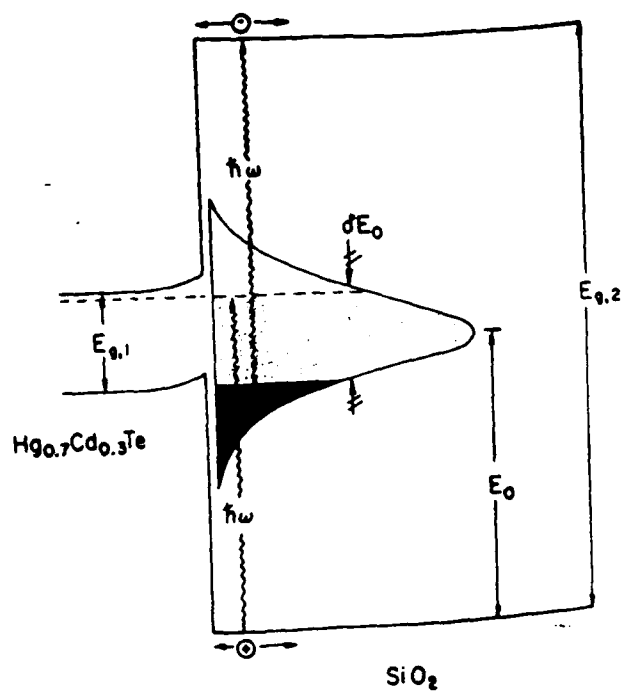


FIG. 34

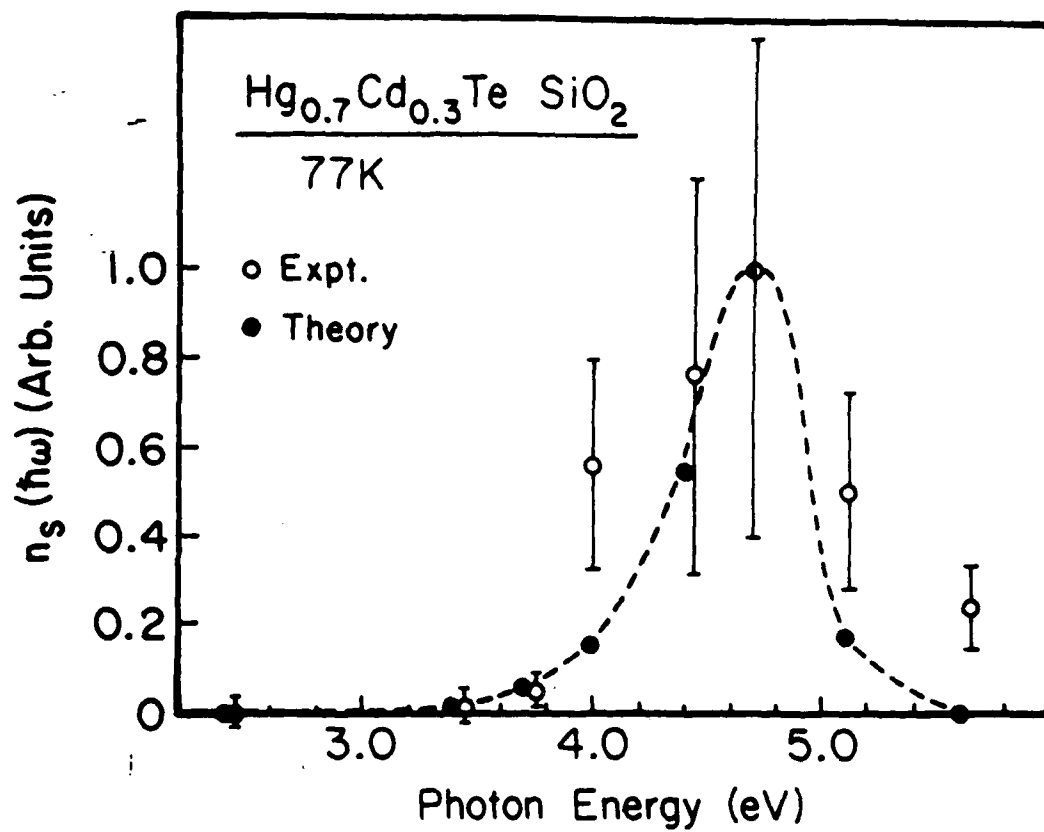


FIG. 35

III. PUBLISHED PAPERS

1. "Raman Spectroscopy and Photoluminescence Study of $\text{Al}_{0.48}\text{In}_{0.52}\text{As}/\text{InP}$ ", A. Ksendzov, P. Parayanthal, F.H. Pollak, D. Welch, G.W. Wicks and L.F. Eastman, Proceedings of the 7th International Conference on Ternary and Multinary Compounds, ed. by S.K. Deb and A. Zunger (Materials Research Society, Pittsburgh, 1987) p. 371.
2. "Raman Spectroscopy Study of $\text{Al}_{0.48}\text{In}_{0.52}\text{InP}$ ", A. Ksendzov, P. Parayanthal, F.H. Pollak, D. Welch, G.W. Wicks and L.F. Eastman, Phys. Rev. B **36**, 7646 (1987).
3. "Raman, Transmission Electron Microscopy and Conductivity Measurements in Molecular Beam Deposited Microcrystalline Si and Ge: A comparative Study", J. Gonzalez-Hernandez, G.H. Azarbayejani, R. Tsu and F.H. Pollak, Appl. Phys. Letts. **47**, 1350 (1985).
4. "Symmetry Forbidden LO-phonon Raman Scattering in Heavily Doped $\langle 100 \rangle$ n-GaAs", H. Shen, P. Parayanthal, F.H. Pollak, R.N. Sacks and G. Hickman, Solid State Comm. **63**, 357 (1987).
5. "Comprehensive Investigation of Polish-Induced Surface Strain in $\langle 100 \rangle$ and $\langle 111 \rangle$ GaAs and InP", Z. Hang, H. Shen and F.H. Pollak, J. Appl. Phys. **64**, 3233 (1988).
6. "Excitation Wavelength and Pump Chopping Frequency Dependence of Photorefectance in $\text{Hg}_{1-x}\text{Cd}_x\text{Te}$ ", A. Ksendzov, F.H. Pollak, P.M. Amirtharaj and J.A. Wilson, J. Crystal Growth **86**, 586 (1988).
7. " $\text{Hg}_{0.7}\text{Cd}_{0.3}\text{Te}/\text{SiO}_2$ -Photox Interface Properties Studied by Photo- and Bias-Induced Charging", A. Ksendzov, F.H. Pollak, J.A. Wilson and V.A. Cotton, J. Crystal Growth **86**, 834 (1988).